

Low-dimensional modelling of a transient cylinder wake using double proper orthogonal decomposition

STEFAN G. SIEGEL¹, JÜRGEN SEIDEL¹, CASEY FAGLEY¹,
D. M. LUCHTENBURG², KELLY COHEN¹
AND THOMAS MCLAUGHLIN¹

¹Department of Aeronautics, US Air Force Academy, HQ USAFA/DFAN, Colorado Springs,
CO 80840, USA

²Institute of Fluid Dynamics and Technical Acoustics, Berlin University of Technology MB1, Straße des
17 Juni 135, D-10623 Berlin, Germany

(Received 29 June 2006 and in revised form 22 April 2008)

For the systematic development of feedback flow controllers, a numerical model that captures the dynamic behaviour of the flow field to be controlled is required. This poses a particular challenge for flow fields where the dynamic behaviour is nonlinear, and the governing equations cannot easily be solved in closed form. This has led to many versions of low-dimensional modelling techniques, which we extend in this work to represent better the impact of actuation on the flow. For the benchmark problem of a circular cylinder wake in the laminar regime, we introduce a novel extension to the proper orthogonal decomposition (POD) procedure that facilitates mode construction from transient data sets. We demonstrate the performance of this new decomposition by applying it to a data set from the development of the limit cycle oscillation of a circular cylinder wake simulation as well as an ensemble of transient forced simulation results. The modes obtained from this decomposition, which we refer to as the double POD (DPOD) method, correctly track the changes of the spatial modes both during the evolution of the limit cycle and when forcing is applied by transverse translation of the cylinder. The mode amplitudes, which are obtained by projecting the original data sets onto the truncated DPOD modes, can be used to construct a dynamic mathematical model of the wake that accurately predicts the wake flow dynamics within the lock-in region at low forcing amplitudes. This low-dimensional model, derived using nonlinear artificial neural network based system identification methods, is robust and accurate and can be used to simulate the dynamic behaviour of the wake flow. We demonstrate this ability not just for unforced and open-loop forced data, but also for a feedback-controlled simulation that leads to a 90% reduction in lift fluctuations. This indicates the possibility of constructing accurate dynamic low-dimensional models for feedback control by using unforced and transient forced data only.

1. Introduction

An important area of work on flow control involves the phenomenon of vortex shedding behind bluff bodies. When the flow separates from a bluff body, the resulting wake exhibits vortex shedding, which leads to a sharp rise in drag, noise and fluid-induced vibration (Gillies 1998). The increased drag is detrimental for vehicle

performance, while vibrations create problems in applications as diverse as stationary ocean platforms, bridges, or automobile antennae. In other applications, the ability to control the wake of a bluff body could be used to increase mixing, e.g. to enhance heat transfer or combustion (von Kármán 1954; Park, Ladd & Hendricks 1993; Roussopoulos 1993).

The flow around these objects of relatively simple geometry can be of astounding complexity, even at modest Reynolds numbers. A prime example of this behaviour is the circular cylinder wake at laminar Reynolds numbers of the order of $Re = 100$. For a comprehensive review of the flow physics, see Williamson (1996). While the von Kármán vortex street is easily observed and visualized, understanding and modelling its dynamics, with the eventual goal of controlling it, are daunting tasks. Ever since von Kármán (1911) first described the formation of the vortices in the wake flow, the vortex street has served as a benchmark for dynamical models that describe its behaviour.

Initially, the motivation for the development of these models was to gain physical understanding. One of the simplest models that emerged early was the Ginzburg–Landau equation, which captures the nonlinear dynamics of a wake-like flow (Park *et al.* 1993). Chomaz, Huerre & Redekopp (1988) and Huerre & Monkewitz (1990) used this equation to demonstrate that the von Kármán vortex street is indeed due to the amplification of a global instability mode, which in turn requires a sufficiently large area of absolute instability in the wake. The first versions of the Ginzburg–Landau equations model only the downstream development of the vortex street, but not the cross-stream flow features. Later extensions developed by Noack, Ohle & Eckelmann (1991), Albaredo & Monkewitz (1992), Roussopoulos & Monkewitz (1996) as well as Papangelou (1992) modelled the transverse flow features as well with variants of the Ginzburg–Landau equations.

More recently, the focus of reduced order model development has shifted from the desire to obtain a physical understanding of the flow field to use of the model for feedback flow control. In this context, a low-dimensional model that is computationally efficient is crucial for several reasons. For the development of control algorithms, a model is required to aid in their derivation. State-of-the-art control theory can only derive controllers for problems with relatively few degrees of freedom. Once a control algorithm has been developed, for the implementation of the control algorithm in an experiment or application, it is necessary to solve the control equations in real-time. This can currently be achieved only for relatively low-complexity controllers.

To achieve the necessary reduction in the order of the modelling problem, proper orthogonal decomposition (POD), also referred to as the Karhunen–Loève decomposition, has been successfully used as a computational tool for reducing the order of the fluid dynamic system. For example, in the case of the two-dimensional circular cylinder wake, a direct numerical solution of sufficient spatial resolution requires of the order of tens of thousands of grid points. Multiplying these by the number of flow variables computed at each grid point leads to a dynamical system with upwards of 10^5 degrees of freedom, a challenging problem, given current control design methods. POD can be used to reduce the order of this problem to a few spatial modes and their corresponding mode amplitudes, which is a size of problem that is within reach of current controls tools.

Low-dimensional model development based on POD decomposition is a three-step process. In the first step, data on the flow field to be modelled is gathered using either numerical or experimental methods. Selection of suitable data sets is a

crucial step in model building and will be discussed in detail below. In the second step, spatial modes and their mode amplitudes are derived from the flow-field data. The most often used approach is the ‘method of snapshots’ developed by Sirovich (1987). Various methods of deciding how to precondition or cluster the data have been suggested in the literature and are discussed below. In conjunction with the spatial POD modes, the associated mode amplitudes may be calculated using an inner product or least-squares-fit approach.

To arrive at a low-dimensional model, the mode set is truncated, usually based on an energy criterion (the eigenvalues in the Karhunen–Loève system represent twice the modal kinetic energy if POD is applied to the velocity field). The third and final step is the development of a model for the remaining mode amplitudes. This is commonly achieved by a Galerkin projection on the Navier–Stokes equations, which yields a system of equations that describes the evolution of the mode amplitudes over time. This set of equations can then be used to develop feedback-control algorithms in a systematic fashion, or to test the performance of control algorithms against this model. All three steps of model development described above involve assumptions and potential problems, with many different solutions proposed in the literature, which we will discuss in the following.

Analysing the aforementioned steps in more detail, a number of workers recognized that POD in its original form is not well suited to describing transient data sets, i.e. data sets that are neither stationary nor periodic in time. In the following, a summary of previous work to remedy the underlying problems is given, with a focus on work aimed at model development. In the first step, selection of the data to be used for modelling, traditionally a small number of snapshots from the time periodic state of the unforced flow have been used. If POD is performed on this limit-cycle data, the resulting spatial modes will represent only the flow field during the limit-cycle oscillations. As was recognized early (e.g. Graham, Peraire & Tang 1999*a, b*), during transient flow behaviour, the ability to describe the instantaneous flow state suffered greatly. Such transients can be simply due to the initial development of the limit cycle in a flow field started from rest, a change of flow condition (e.g. Reynolds number) or, more importantly in the flow-control context, can be induced by open- or closed-loop forcing.

Consequently, more than one flow condition is required in order to successfully model a flow field which undergoes transient development. Noack *et al.* (2003) proposed to use the steady solution of the flow as an additional data point in order to achieve a model with correct transient dynamics. Siegel *et al.* (2005) demonstrate that the inclusion of transient forced data can be used to construct a mode basis that also includes forcing effects on the flow field. Bergmann, Cordier & Brancher (2005) employ a chirp signal to force the flow into different states thus enlarging the data basis used for model construction. Afanasiev & Hinze (2001) use POD in an iterative fashion to keep the model valid as the flow changes.

Another problem pertains to biasing of the POD modes owing to data selection. Since POD is an energy optimal procedure, and it is usually desirable to use snapshots from different flow conditions for model building as detailed in the previous section, the resulting spatial POD modes will vary greatly if the number of snapshots from two different flow states (e.g. Reynolds number) is varied more towards one or the other flow state. This problem is aggravated if transient data is used, and different transients yield a different number of snapshots. Taylor & Glauser (2004) describe this effect and some attempts to resolve it. Jørgensen, Sørensen & Brøns (2003) describe a method they refer to as sequential POD to process data from different flow

states while producing orthogonal POD modes for a cavity flow. Although not energy optimal, this sequential POD procedure represents the dynamic behaviour better than regular POD according to the authors and by design the POD modes constitute an orthogonal basis.

In an attempt to overcome this problem for the cylinder wake, Noack *et al.* (2003) as well as Siegel, Cohen & McLaughlin (2003) noted independently that the main error encountered in the case of a cylinder wake is due to the change of the mean flow, in particular, the change of the length of the recirculation zone. This led to the addition of a so called ‘shift mode’ (Gerhard *et al.* 2003) or ‘mean flow mode’ (Siegel *et al.* 2003), which was motivated by the mean-field theory developed by Stuart (1958) (see Noack *et al.* 2003). The shift mode in essence adds one degree of freedom to the model, which enables the model to account for changes of the length of the recirculation zone. As a result, the model error is greatly reduced during off-design start-up conditions, and the numerical stability of the model is improved as well. The model with the additional shift mode was successfully employed by Zielinska & Wesfreid (1995) for experiments and in simulations by Morzynski *et al.* (2006).

While the additional mode alleviated some of the problems observed during cylinder wake start-up simulations, the changes in the spatial POD modes that represent the fluctuations, especially the von Kármán vortex modes, are still not captured by this approach, and the transient dynamics of the model still do not match the results from the Navier–Stokes simulations in terms of the initial growth rates (Noack *et al.* 2003). Realizing this problem, Noack *et al.* (2003) added spatial modes obtained from a linear stability analysis to their set of POD derived modes used for low-dimensional model development. These stability modes were added based on the notion that the initial development of the vortex street can be described accurately by linear theory. The resulting transient dynamic behaviour predicted by the model showed a vast improvement over earlier models and the results are in good agreement with those obtained by direct numerical simulations. This development is a further indication that the main issue in developing dynamically accurate low-dimensional models lies in obtaining a mode set that spans the entire parameter range of interest. However, obtaining stability modes for any flow field is no easy task, and there is no guarantee that it is possible to obtain these modes for more general three-dimensional flow fields (see also Graham *et al.* 1999*a, b*).

In essence, the POD modes either fail to cover the dynamic behaviour of the flow well if all available data from different flow conditions are processed *en bloc* (Jørgensen *et al.* 2003), or the resulting modes are no longer orthogonal if the data from different flow conditions are processed separately, which at a minimum requires further processing steps. One approach was used by Morzynski *et al.* (2006) and Luchtenburg *et al.* (2006), who employed an interpolation scheme to cover flow states that are between the flow states used for mode derivation, thus allowing for a model that covers transient dynamic effects. Other approaches to precondition data before processing it using POD have been successfully used as well. Ma & Karniadakis (2002) used a modelling approach for a three-dimensional cylinder wake that uses both two- and three-dimensional modes in order to capture the spanwise behaviour of the flow correctly. They also derived modes from different Reynolds-number flow fields in order to build models that correctly model the bifurcation from two- to three-dimensional flow behaviour. While all of the attempts to precondition data before processing them with POD described so far were aiming at *a priori* enlarging the mode basis to cover a broader set of flow conditions, a second fundamentally

different approach to maintaining modal validity for changing flow conditions has also been reported. Referred to as trust region POD, the idea is to check on the validity of the POD model while the flow is changing, and to recalculate the POD basis once the modes are found to be inaccurate. Introduced initially by Fahl (2000), Bergmann & Cordier (2006) employed this method to control the circular cylinder wake. Although the resulting optimization problem is simpler, an iterative approach with recalculation of the POD modes is required. This also applies to Ravindran (2000) who used a POD based model that is periodically updated to extend its range of validity. Sirisup *et al.* (2005) employed a similar equation-free method that updates the POD based model periodically with CFD simulation data, and reported this approach to be less sensitive to changes in Reynolds number.

In the third step of model development, the resulting mode amplitudes from the POD procedure must be described in terms of their dynamic behaviour using a set of equations. An established method for deriving a set of equations based on POD modes is the use of a Galerkin projection, where the truncated POD results are projected onto the Navier–Stokes equations. While mathematically valid, the resulting equations are a point design and the initial set of equations is often structurally unstable when integrated numerically (Noack *et al.* 2003). This structural instability has been described by Deane *et al.* (1991) as well as by Rempfer (2000), who provides an explanation for this instability. Stuart (1958) described a method to solve this instability problem, and recently developed models that take this approach into consideration arrive at structurally stable models (Noack *et al.* 2003). However, for all Galerkin models, the implementation of the actuation into the model is a major challenge, and is often limited to the addition of a linear term that must be calibrated using experimental or computational data. The advantage of calibration is that it negates the need for spatial derivatives, which can cause problems when data uncertainty is present. Calibration has been successfully employed by Galletti *et al.* (2004) as well as Noack, Tadmor & Morzynski (2004*b*). Alternatives to the use of Galerkin projection have also been investigated. Narayanan *et al.* (1999) employ an artificial neural network as an alternative method to using a Galerkin projection. They report that this ANN approach models both the short- and long-term flow features of a diffuser flow, however, the model develops phase errors over longer time spans. Khibnik *et al.* (2000) continue the work of Narayanan *et al.* (1999), commenting on the complementary nature of both ANN- and Galerkin-based models. Sahan *et al.* (1997) compared ANN- and Galerkin-based projections to develop low-dimensional models based on POD mode amplitudes for a grooved channel flow. They find that, ‘The use of ANNs in order to emulate the dynamical behaviour of the flow system combines all the benefits of the Galerkin Projection based low order models with the parallel and fast processing capabilities of neural networks’.

While some of the publications discussed in the previous section employ an ANN in order to develop a low-dimensional model of the flow, the more widespread use of ANNs in flow control consists of direct mapping of flow measurements to actuator control signals in the context of feedback flow control. Gad-el-Hak (2000) states that, ‘For flow-control applications, neural networks offer the possibility of adaptive controllers that are simpler and potentially less sensitive to parameter variations as compared with conventional controllers.’ Many examples of this use of neural networks exist and the work of Fan, Hofmann & Herbert (1993), Fan (1995), Pindera (2002), Lee *et al.* (1997) may serve as examples for computational work employing neural networks for feedback control purposes. Gillies (1995, 1998, 2000) employs an ANN-ARX model as a one-step predictor for the POD mode amplitudes in order

to close the feedback control loop to control a reduced-order model of the circular cylinder wake at $Re = 100$. Examples of experimental work employing neural networks to map sensor readings to actuator commands are Faller, Schreck, & Luttgies (1995), Faller & Schreck (1997), Hočevár, Širok, & Grabec (2004) as well as Efe *et al.* (2004, 2005). The main drawback inherent in this model-free approach is the lack of a global flow estimation, which is not achieved when only individual sensor readings are processed without a model in order to obtain a control command.

The importance of a model that is valid for all flow conditions encountered during feedback lies in the ability to stably control the flow. There are numerous records in the literature about control instabilities resulting from the inability of the model to represent and estimate the flow correctly, for example Siegel *et al.* (2003) and Tadmor *et al.* (2004). It is often difficult to pinpoint the problem in these cases, which may either lie in the model or the controller itself. Thus, a thorough evaluation and validation of a reduced-order model is crucial, especially when it is used for controller development or evaluation.

In summary, we find room for improvement in all three steps of model development. This is necessary to develop low-dimensional flow models based on limited amounts of flow field data that are both robust and accurate. It is neither possible nor necessary to obtain flow data for all possible initial and forcing conditions; however, data from more than just the unforced flow state must be collected for a useful dynamic model of a flow field. This requirement is not just backed by recent experiences gathered in feedback flow control, but has been well established in the structure controls community. In this work, we combine the main advantage of POD, namely its optimality and thus its ability to capture the global behaviour of a flow field with a minimum number of modes, with established system identification techniques originally developed for the control of flexible structures and the modelling of dynamical systems. Over the past few decades, the controls community has developed methods to identify the dynamic properties of complex structures based on experimental measurements. These rely on the acquisition of transient measurements based on a known excitation input to the system. System identification methods are then used to develop a dynamical mathematical model that can be used later for design and analysis of an effective control law as well as for dynamic observer development. We adapt this approach in this work, but implement POD into the development path in order to capture the global spatial flow behaviour.

This paper is structured as follows. We first describe the numerical set-up to obtain the flow-field data required for modelling in §2. In §3, we then discuss the mathematical description of the modified POD procedure which we refer to as double proper orthogonal decomposition or DPOD. In §4, the fluid dynamic phenomena observed in the cylinder wake are described and DPOD is used to develop transient spatial mode sets and demonstrate the truncation as well as estimation error results. Using the DPOD mode amplitudes, in §5 we describe the low-dimensional modelling approach used to represent the time-dependent mode amplitudes of the POD modes. Our approach is based on a nonlinear system identification approach using artificial neural networks (ANN). Finally, in §6, we examine this dynamical model in terms of robustness for various sets of open-loop forced excitations which were not used during model development. Also, the performance of the model at off-design Reynolds numbers is investigated. The ultimate test for the usability of the model for feedback-flow-control applications is performed by supplying the forcing input from a feedback-controlled simulation to the model and comparing the results to the solution of the CFD simulation.

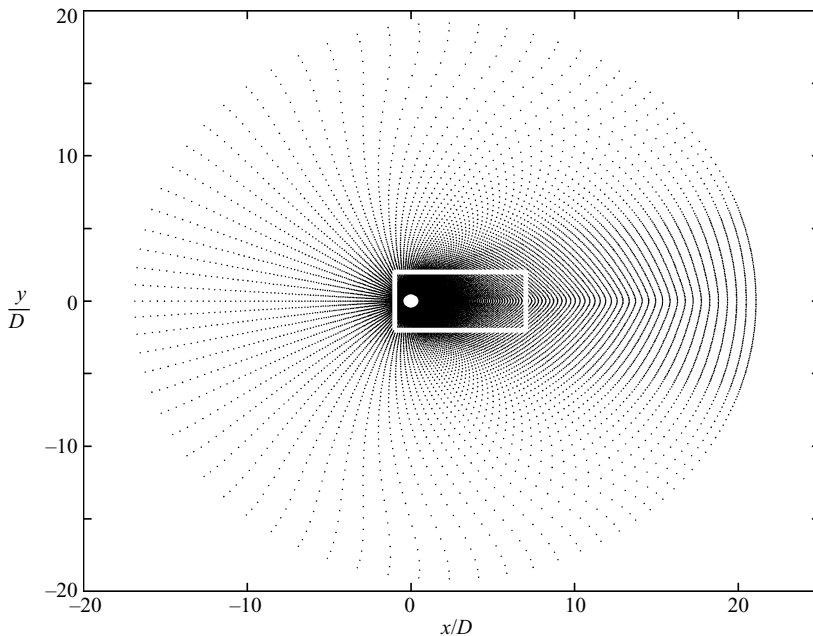


FIGURE 1. Computational grid points (.) and POD domain boundary (white solid line). The POD domain extends from $x/D = -1$ to 7 in the streamwise direction, and from $y/D = -2.5$ to 2.5 in the flow normal direction.

2. Simulation set-up

For the numerical simulations, the commercial finite-volume code Cobalt, solving the compressible Navier–Stokes equations (Strang, Tomaro & Grismer 1999), was used. The numerical method is a cell-centred finite-volume approach applicable to arbitrary cell topologies (e.g. hexahedra, prisms, tetrahedral). The spatial operator uses the exact Riemann solver of Gottlieb & Groth (1988), least-squares gradient calculations using QR factorization to provide second-order accuracy in space, and TVD flux limiters. A point implicit method using analytic first-order inviscid and viscous Jacobians is used for advancement of the discretized system. For time-accurate computations, a Newton sub-iteration scheme is employed, and the method is second-order accurate in time.

Boundary conditions at the far field are implemented as Riemann invariants. The cylinder surface is modelled as an adiabatic non-slip surface. Transverse body translation was used as forcing input to obtain open-loop forced data sets. Rigid-body motion is achieved through an arbitrary Lagrangian Eulerian (ALE) formulation, where the grid is neither stationary nor follows the fluid motion. The conservation equations are solved in an inertial reference frame, but the spatial operator is modified so that the advection terms are relative to the (non-inertial) grid reference frame. A number of Newton sub-iterations are used to reduce errors associated with integrating over the time step with an implicit temporal operator.

For all investigations presented here, a structured two-dimensional grid with 63 700 nodes and 31 752 elements was used (figure 1). The grid extended from -16.9 cylinder diameters to 21.1 cylinder diameters in the (streamwise) x -direction, and ± 19.4 cylinder diameters in (flow normal) y -direction, with the origin located at the cylinder centre. During simulation, data were collected only within the POD spatial domain extending

from $x/D = -1$ to $x/D = 7$ in the streamwise direction, and from $y/D = -2.5$ to $y/D = 2.5$ in the flow normal direction. This resulted in about 21 000 spatial sampling locations used to calculate POD modes.

Other pertinent simulation parameters (see the *Cobalt User's Manual*† for more details):

Reynolds number $Re = 100$;

Damping coefficients: advection = 0.01; diffusion = 0.00;

32 Iterations for matrix solution scheme;

3 Newtonian sub-iterations;

Non-dimensional time step $\Delta t^* = \Delta t(U/D) = 0.05$.

The unsteadiness in the simulations was triggered by initially skewing the incoming flow by $\alpha = 0.5^\circ$ in order to introduce an initial perturbation. A grid and time resolution study showed good convergence for the simulation parameters outlined above. For further validation of the unforced cylinder wake CFD model at $Re = 100$, the resulting value of the mean drag coefficient, c_d , was compared to experimental and computational investigations reported in the literature. At $Re = 100$, experimental data, reported by Oertel (1990) and Panton (1996), point to c_d values ranging from 1.26 to 1.4. Furthermore, Min & Choi (1999) report several numerical studies that obtained drag coefficients between 1.34 and 1.35. The COBALT CFD model used in this effort resulted in a value of $c_{d0} = 1.35$, which compares well with the values in the literature. Another important benchmark parameter is the Strouhal number ($St = f * D/U$), which is the non-dimensional vortex shedding frequency for the unforced cylinder wake. Experimental results at $Re = 100$, presented by Williamson (1996), show Strouhal numbers ranging from 0.163 to 0.166. The Strouhal number obtained in this effort is $St = 0.163$, which also compares well. The non-dimensional time step in connection with the natural shedding frequency yielded about 100 CFD time steps per unforced shedding cycle. This was further reduced by down sampling to 20 snapshots per cycle which were then used as input to the DPOD procedure described in the following.

3. Extensions to proper orthogonal decomposition

The proper orthogonal decomposition (POD) of a two-dimensional scalar spatial field u evolving over time can be written as (Holmes, Lumley & Berkooz 1996)

$$u(x, y, t) = \sum_{j=1}^{\infty} a_j(t) \varphi_j(x, y). \quad (3.1)$$

Here, $a_j(t)$ are the mode amplitudes of the spatial modes $\varphi_j(x, y)$. For practical applications, formulating the problem using the method of snapshots (Sirovich 1987) proves to be advantageous. While this decomposition yields as many modes as there are snapshots in the original data set, it is typically possible to truncate the POD model at a relatively low number of modes while retaining most of the energy of the original flow field. This can be done by either inspecting the energy distribution in the modes, or by inspection of the spatial modes, which typically will not show any discernible structure beyond a certain mode number j . If POD is performed on the flow field without subtracting the mean flow, the first mode will be the mean flow, followed by modes representing the large-scale fluctuations in the flow field. In the case

† Cobalt Solutions, LLC, www.cobaltcfd.com.

of the cylinder wake, the largest fluctuating modes are the two modes representing the von Kármán vortex street. Since in almost all cases the modes obtained by POD describe the main features of the flow, we will refer to them as the *main modes*. The decomposition works particularly well for flow fields with large time-periodic features such as the periodic vortex shedding in wake flows.

3.1. Short time proper orthogonal decomposition (SPOD)

Gillies (1995) and Siegel *et al.* (2005) have shown that for time-periodic flows, modes identical to those obtained from snapshot ensembles containing a large number, of shedding cycles can be obtained using snapshot ensembles of small integer numbers, of cycles, down to a minimum of one shedding cycle. A similar idea to extend POD has been developed by Glezer, Kadioglu & Pearlstein (1989) for flows that are not statistically stationary. Siegel *et al.* (2005) demonstrate that the difference between a spatial mode obtained from integer numbers of shedding cycles is minimal compared to a POD decomposition obtained from a large number (in the limit infinite) of shedding cycles. Similar behaviour is observed in a fast Fourier transformation (FFT). While in an FFT the error due to non-integer numbers of cycles can be alleviated using windowing functions, this approach does not appear to work for POD decompositions (Siegel *et al.* 2005). Siegel *et al.* (2005) refer to POD of only a single oscillation cycle as short-time POD or SPOD, owing to its similarity to procedures such as short-time Fourier decomposition.

SPOD allows for a decomposition of time-evolving flow fields with some approximate periodicity into (k) individual events of exactly one cycle of the dominant frequency,

$$u^{(k)}(x, y, t) = \sum_{i=1}^I a_i^{(k)}(t) \varphi_i^{(k)}(x, y). \quad (3.2)$$

The result is a collection of K cycles in individual bins. Note that these bins may contain a different number of samples in time, or span slightly varying time intervals as the period of a cycle changes. However, since SPOD yields K bins of spatial POD modes that are valid for one individual cycle of a transient flow change, it is not as low-dimensional as we would wish. The result of SPOD is one entire mode set for each period of the flow. It should also be noted that modes obtained from an individual cycle are *a priori* not orthogonal to modes from other cycles. In fact, if the data are completely periodic, the modes obtained from different bins are identical if the number of snapshots is constant per cycle.

3.2. Double proper orthogonal decomposition (DPOD)

Building on the resulting spatial modes of a SPOD decomposition, we could conceive the following mode construction procedure: if the modes in two consecutive cycles vary only slightly, it should be possible to obtain a representation of the modes of the second cycle as the corresponding mode of the first cycle plus a small shift. This procedure, borne from the aforementioned ‘mean flow mode’ or ‘shift mode’ idea, can be formalized by realizing that mode i of all bins (k) from the SPOD procedure can be viewed as the input to a second POD (the bins now act similarly to time above) as follows:

$$\varphi_i^{(k)}(x, y) = \sum_{j=1}^J w_{ij}^{(k)} \Phi_{ij}(x, y). \quad (3.3)$$

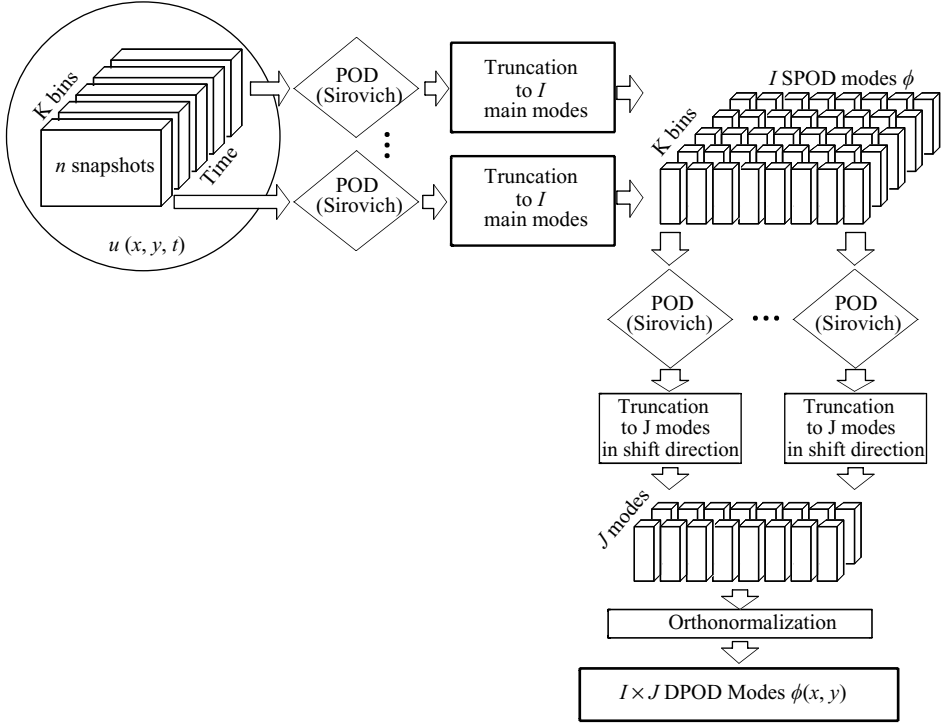


FIGURE 2. Flowchart of DPOD decomposition process.

This leads again to an optimal representation of all SPOD main modes i . Equation (3.4) summarizes the double POD (DPOD) decomposition of the velocity field u :

$$u(x, y, t) = \sum_{i=1}^I \sum_{j=1}^J a_{ij}(t) \Phi_{ij}(x, y) \quad (3.4)$$

This DPOD formulation takes the concept of the ‘shift mode’ one step further: we can now develop a ‘shift mode’, even a series of higher-order shift modes, for all main modes i by applying the POD procedure to the POD mode sets $\phi_i^{(k)}$. The resulting mode ensemble in its untruncated form has as many main modes I as there were snapshots in the smallest SPOD bin, and as many shift modes J as there were bins. It can then be truncated in both i and j , leading to a mode ensemble that is $I_M \times J_M$ in size. We will thus refer to the size of the truncated DPOD mode sets by indicating the truncation indices $I_M \times J_M$ in the following. A pictorial representation of the DPOD procedure is given in figure 2. Starting in the top left-hand corner, the data are split into K bins and each bin is used as an input data set for its individual POD procedure. The resulting SPOD modes are then collected *across the bins* and POD is applied again to obtain the shift modes.

The resulting eigenfunctions can be truncated in both I and J in the same way as a regular POD decomposition. After orthonormalization, the decomposition is again optimal in the sense of POD. In the limit of $J = 1$, the original POD decomposition is recovered. While the different modes distinguished by the index i remain the *main modes* described above, the index j identifies the transient changes of these main modes: For $J > 1$, the energy optimality of the POD decomposition in that direction

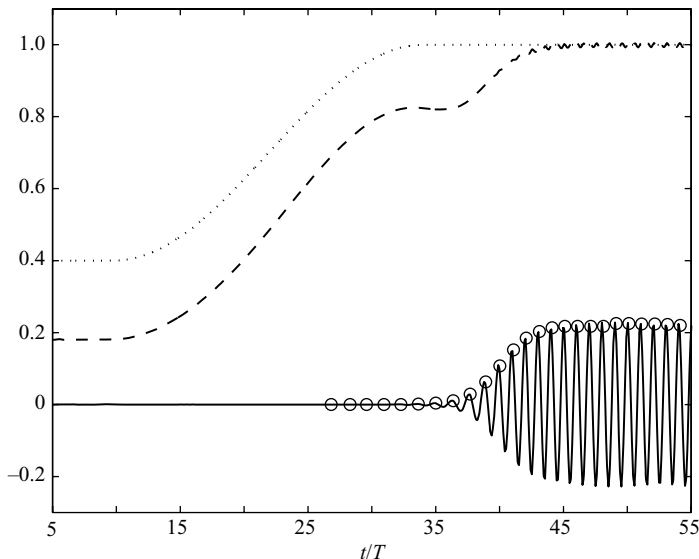


FIGURE 3. Normalized lift (C_L/C_{D0} , —) and drag (C_D/C_{D0} , - -) coefficients during evolution of the limit cycle oscillation. The Reynolds number ($Re/100$, ...) is ramped from 40 to 100 as shown. The SPOD segmentation times are indicated by circles.

leads to modes that are the optimum decomposition of a given main mode as it evolves throughout a transient data set. If $J=2$, then modes $\Phi_{1,1}$ and $\Phi_{1,2}$ are similar to the mean flow and its ‘shift mode’ or ‘mean flow mode’ as described by Noack *et al.* (2003) and Siegel *et al.* (2003), respectively. Thus the modes with indices $j > 1$ can be referred to as first, second and higher-order ‘shift’ modes that allow the POD mode ensemble to adjust for changes in the spatial modes. We will refer to all of these additional modes obtained by the DPOD decomposition as *shift modes*, since they modify a given *main mode* to match a new flow state due to either a recirculation zone length or formation length change. This may be due to effects of forcing, a different Reynolds number, feedback or open-loop control or similar events. Thus, in the truncated DPOD mode ensemble for each main mode, one or more shift modes may be retained based on inspection of energy content or spatial structure of the mode.

In the following, we will demonstrate how this DPOD procedure can be used to create mode ensembles that cover both the unforced time-periodic vortex-shedding state of the circular cylinder wake, as well as the low-amplitude forced flow within the lock-in region. This mode ensemble will thus cover not just the limit cycle, but also the influence of forcing onto the vortex-shedding process.

4. Application of DPOD to cylinder wake data

4.1. Start-up transient

The von Kármán vortex street develops as the result of global flow instability (Williamson 1996). This transient development of the oscillatory limit cycle starts when a closed recirculation zone forms downstream of the cylinder that is steady in time for Reynolds numbers smaller than $Re_c = 47$. On increasing the Reynolds number, this unstable flow field starts to exhibit vortex shedding, which increases in strength over several shedding cycles as evidenced by the fluctuations in the lift force as shown in figure 3. During this transient start-up, both the shedding frequency and

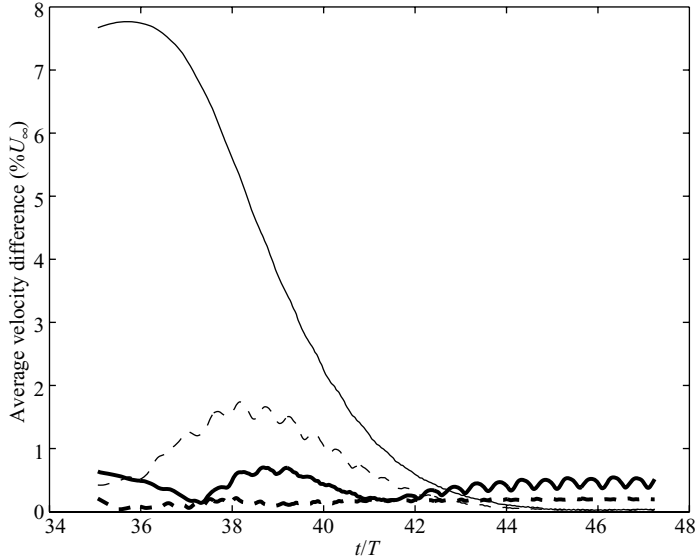


FIGURE 4. Average reconstructed flow field r.m.s. estimation error of differently truncated mode sets for the simulation data of the transient development of the limit cycle. Ten POD modes derived from time periodic flow (thin solid line), 10 POD modes derived from time periodic flow plus shift mode (thin dashed line), 5×2 DPOD modes (thick solid line), 5×3 DPOD modes (thick dashed line).

the strength of the shed vortices change. By starting a CFD simulation at a Reynolds number below this threshold ($Re = 40$ in our case), and subsequently ramping up the flow speed to the target Reynolds number of $Re = 100$, we can study the details of the development of the limit cycle. The ramping was done smoothly using a constant acceleration, and no numerical artefacts were observed during the transition.

The traditional approach to development of a set of POD modes uses data from one or several shedding cycles of the fully developed nonlinearly saturated limit cycle, i.e. data from later than about $t/T = 55$ into the simulation shown in figure 3. Although this set of POD modes models the limit cycle extremely well, it can be seen in figure 4 that an increasing estimation error in terms of the L2 norm results when data sets taken during the transient start-up of the shedding are mapped onto these spatial modes. The POD spatial mode ensemble was truncated here at 10 modes, but the estimation error remains unaffected when more spatial modes are retained. The reason for this large estimation error lies in the drastic changes of both the mean flow and the formation length during the transient start-up. The length of the recirculation zone, which extends initially to about 5 cylinder diameters downstream of the cylinder centre, shortens to about 2.5 cylinder diameters once the limit cycle is fully developed. The formation length (Williamson 1996), equivalent to the location of the maximum velocity fluctuations, changes in a similar fashion.

The change in mean flow can be compensated for by the addition of an artificially created ‘shift’ (Gerhard *et al.* 2003) or ‘mean flow’ (Siegel *et al.* 2003) mode, which allows the length of the recirculation zone to adjust. This addition to the mode set greatly reduces the estimation error, as seen in figure 4. However, the fluctuating modes are unchanged, and thus the formation length is only correctly modelled for the limit cycle. Since there is no unsteadiness initially, the model including the shift mode shows small errors both for the steady recirculation zone flow at the beginning of the

start-up transient, and for the limit cycle that was used to derive the spatial POD fluctuating modes. In between these states, however, the model shows a significant error caused by the inability of the fluctuating modes to track the change of the formation length correctly during start-up. Since this exchange of energy between the fluctuating modes and the mean flow dominates the start-up dynamics, the POD model with shift mode only (referred to in Noack *et al.* 2003 as Model B) cannot possibly capture the dynamics of the start-up transient correctly, as was shown in figure 12 of Noack *et al.* (2003). However, the effects of formation length change may be correctly included in a low-dimensional model by adding modes that capture this behaviour. Noack *et al.* (2003) achieve this using stability modes derived from a global stability analysis of the steady solution of the flow. In this work, we will demonstrate a systematic approach to achieve the same effect, using the DPOD decomposition detailed below.

Processing the same data set using the DPOD procedure, we can obtain a 10 or 15 mode model by retaining five main modes and either one or two shift modes for each main mode. The spatial POD modes of the 5×2 mode model are shown in figure 5. To obtain these modes, separate POD decompositions were performed for 11 independent snapshot ensembles consisting of exactly one shedding cycle each. The shedding cycles were determined using a peak-detection algorithm applied to the lift force shown in figure 3 and are indicated by circles. Since the temporal sampling rate remained the same at about 20 snapshots per shedding cycle of the time periodic flow, the initial bins contain more snapshots owing to the longer period than the time-periodic flow bins. The resulting POD mode ensembles were truncated to retain five main modes each ($I = 5$) and subjected to a second POD decomposition performed on a given main mode from all snapshot ensembles, i.e. on the 11 different modes 1, modes 2, and so on. The results of this second POD decomposition were truncated at either two or three modes for the 5×2 or 5×3 mode model, respectively. The truncated DPOD spatial mode basis was then orthonormalized. Comparing the DPOD-based estimation errors for both models (figure 4), it can be seen that the maximum of the estimation error during the entire start-up transient is reduced to well below 1% for the 5×2 mode model, and a fraction of 1% with an almost flat distribution for the entire start-up transient for the 5×3 mode model. It should be noted that the DPOD models, if not truncated, will recover the exact data set used for their derivation, just as the traditional POD models. Inspecting the DPOD spatial modes shown in figure 5 in more detail, it can be seen that mode $i = 1, j = 1$ is the mean flow, followed by modes $i = 2, j = 1$ and $i = 3, j = 1$ as the Kármán vortex-shedding modes. These modes together contain more than 90% of the fluctuation energy of the limit cycle. The normalized energy content of the DPOD modes is shown in figure 6. Modes $i = 4, j = 1$ and $i = 5, j = 1$ are a higher-order harmonic mode, with about 4% of the fluctuation kinetic energy in each mode. While not identical, modes $i = 1, j = 1$ to $i = 1, j = 5$ are similar to the mean flow and the first four modes of a regular POD decomposition performed on limit cycle data. Mode $i = 1, j = 2$, which is the shift mode of the mean flow, is very similar and serves the same purpose as the shift mode constructed by Noack *et al.* (2003) or Siegel *et al.* (2003). The main improvement of DPOD, however, lies in the shift modes obtained for the main von Kármán vortex-shedding and higher modes, modes $i = 2, j = 2$ to $i = 2, j = 5$. Comparing the minima and maxima of a given fluctuating spatial mode and its shift mode, we can see that mode and shift mode are out of phase close to the body, and in phase far downstream. Thus, adding a main mode and its shift mode with the same phase will result in weaker peaks close to the cylinder, and

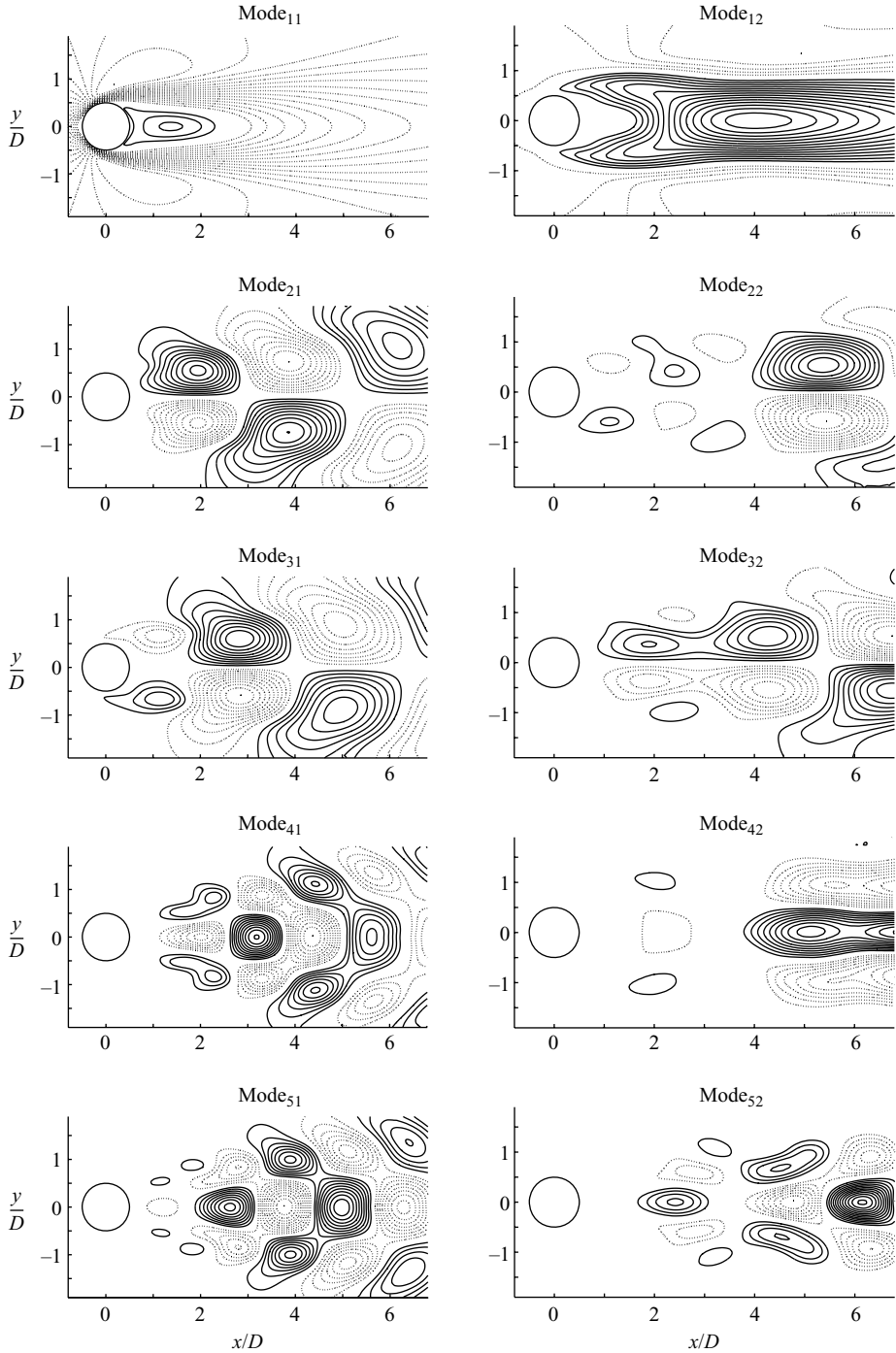


FIGURE 5. Truncated spatial mode set for transient development of the limit cycle flow field showing 5×2 DPOD modes. The first shift modes are in the right-hand column, the main modes in the left. Dashed lines are negative iso-contours of streamwise velocity, solid lines positive iso-contours.

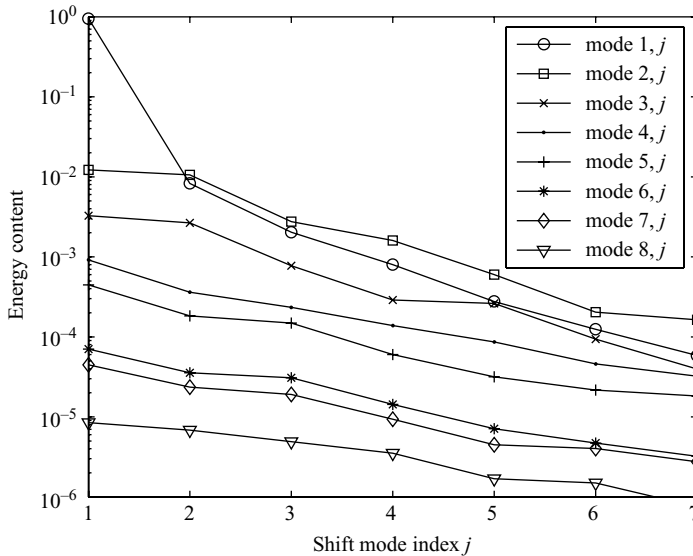


FIGURE 6. Energy content for the DPOD model developed from transient Reynolds number ($Re = 40$ to 100 data shown in figure 2), as well as transient open-loop forced data.

stronger peaks farther downstream. This is a situation encountered during the onset of vortex shedding, where the formation length is relatively large. Considering the mode amplitudes of a given fluctuating mode and its shift mode shown in figure 7, it can be seen that at the beginning of the simulation the amplitudes of the modes and their shift modes are in phase. This correctly models the long formation length observed in inspecting the original data. However, around $t/T = 9$, the shift mode amplitudes experience a phase reversal with respect to their respective main mode amplitudes, and from then on remain 180° out of phase. This effectively results in a subtraction of the spatial mode and its corresponding shift mode, which results in stronger modal peaks close to the cylinder, and weaker peaks further downstream. This correctly models the flow state encountered during the limit cycle, where the formation length is shorter and the vortices form closer to the cylinder. We conclude from these observations that the shift modes obtained from the DPOD procedure achieve the same purpose for adjusting the formation length as the mean flow shift mode does for the mean flow: it allows the POD model to correctly capture the changes encountered during transient flow situations.

4.2. Transient forced simulations

With these encouraging results in modelling unforced flow behaviour, we proceed to examine the effectiveness of the DPOD procedure in modelling the transient behaviour of open-loop forced flow fields. The effect of cylinder translation on the vortex shedding behind a circular cylinder has been investigated in the literature in detail, starting with the investigations of Koopmann (1967). The parameter space is two-dimensional considering both the non-dimensional peak cylinder displacement, A/D , and the forcing frequency normalized by the natural shedding frequency f_0 , $(f - f_0)/f_0$. Figure 8 shows the results of Koopmann (1967) indicating the so-called lock-in region, within which the vortex shedding exhibits a fixed phase relationship with the forcing. Outside of this lock-in region, the flow response to the forcing is chaotic. The question is now how well (if at all) a DPOD model can capture the wake

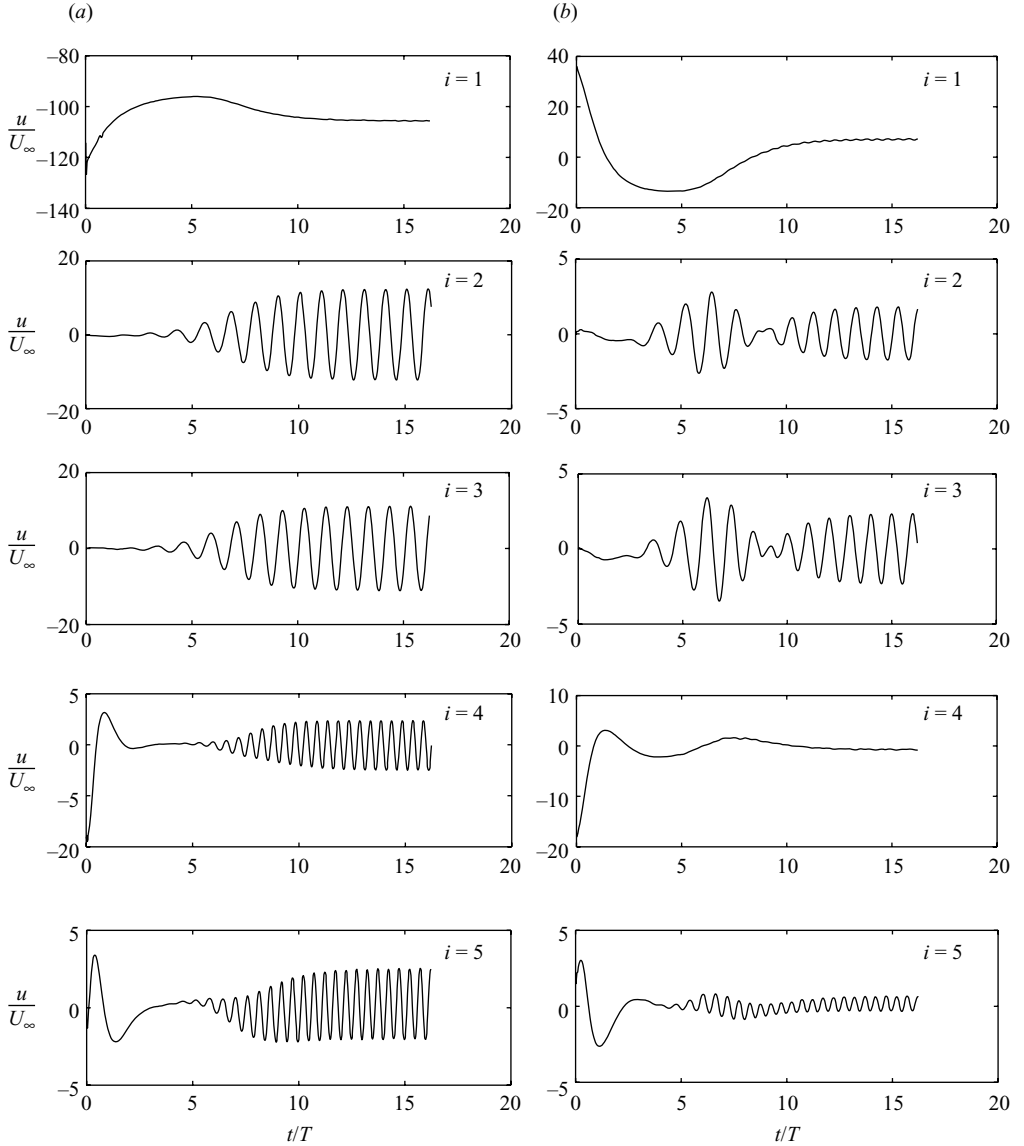


FIGURE 7. Mode amplitudes a_{ij} of the first 5×2 DPOD modes during transient development of the unforced cylinder wake limit cycle, $Re = 100$. For corresponding spatial modes, refer to figure 5. (a) $j = 1$, (b) $j = 2$.

behaviour within this lock-in region, given only a limited number of simulations with which to develop the model. Of particular interest is the question of whether the DPOD model will yield usable flow-field estimates for data sets that were not used for the development of the spatial modes. Note that in the transient start-up model development presented above, the flow field used for model development and for state estimation were identical.

For the transient forced flow-field investigations, we employ five simulation data sets obtained for different forcing conditions (figure 8) to derive a set of spatial DPOD modes. We then proceed to project the snapshot data onto these spatial modes to derive the mode amplitudes not just for the data sets from which they were obtained,

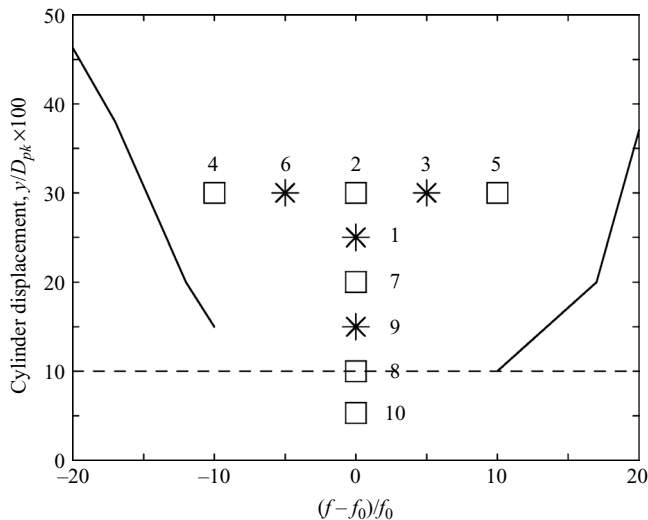


FIGURE 8. CFD simulation data sets used for mode set derivation and mode set verification. Solid lines indicate the limits of the lock-in boundary as identified by Koopman (1967). Data sets identified by a square are used for spatial mode derivation. Data sets identified by stars are used for mode verification. The case numbers are referenced in the text and in table 3.

but also for four additional data sets within the lock-in region that were not used for the spatial mode development. The rationale behind this is to test the robustness of the model for off-design conditions: even within a parameter space that is only two-dimensional, it is impossible to include all possible combinations of forcing parameters in the model development. Thus, it is of interest to know how much information is required in order to yield a stable and accurate flow model for an entire range of forcing conditions, in this case, for the lock-in region at small amplitudes.

The simulations for obtaining open-loop forced data were restarted with the flow solution from the end of the unforced limit cycle simulation presented above. In order to prevent non-physical transients in the flow, the cylinder displacement was prescribed as a C^2 continuous function $y_c(t)$. The forcing was started exactly out of phase with the vortex shedding, which yields the longest possible transient while the phase of the shedding adjusts to the phase of the forcing, and was applied for 15 periods of the forcing frequency. A typical forcing signal is shown in figure 9(a). The flow response to the forcing is dependent on both the amplitude and the frequency of the forcing; in general, the smaller the forcing amplitude, the longer the transient after activation of the forcing. Figure 9(b) shows the transient for the particular forcing conditions to last for about 10 shedding cycles before a stable phase relationship between forcing and vortex shedding is established. The unsteady lift coefficient in this phase-locked state is larger than in the unforced flow field, indicating stronger vortex shedding, which results in an increase in the drag coefficient c_D as well. While shown for one forcing condition only, all open-loop forced cases investigated show this behaviour, even though the amount of increase in lift fluctuations and drag coefficient varies for different forcing parameters. After the forcing is stopped, the flow resumes its original shedding pattern, indicated by a return of lift fluctuations and drag coefficient to the unforced values. The amount of time that this second transient lasts, again depends on the forcing parameters. Both transient phases yield important information on the dynamics of the flow and its interaction with the forcing.

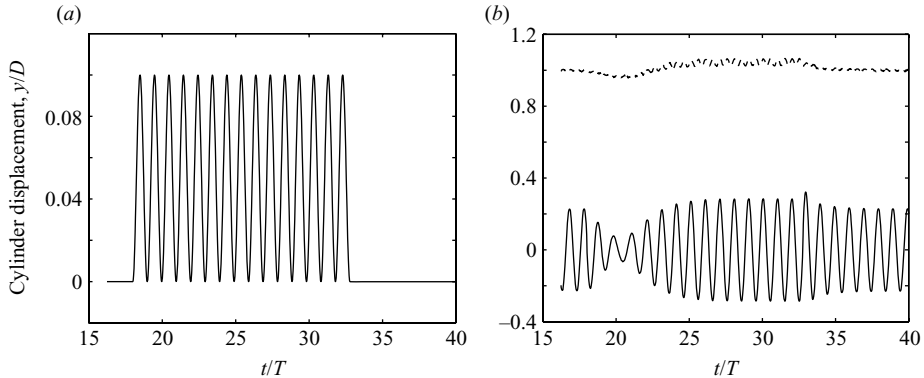


FIGURE 9. (a) Cylinder displacement. $f/f_0 = 1$; $A/D = 0.05$. Forcing activated at $t/T = 18$ and stopped at $t/T = 33$, after 15 full forcing cycles. (b) Transient forced normalized lift coefficient c_l/c_{l0} (solid line) and drag coefficients c_d/c_{d0} (dashed line).

The goal of developing a low-dimensional model is to capture the flow behaviour in these situations accurately, not just for the unforced and periodically forced flow states. The first step towards this goal is to develop a spatial mode set that is able to represent the flow state correctly during all phases, unforced, forced and transient. In order to achieve this, DPOD was applied to the six simulation runs indicated in figure 8 just as for the unforced start-up simulation presented above. The DPOD decomposition was truncated at 3 main modes (consisting of the mean flow and the von Kármán modes) and one shift mode, yielding the total DPOD mode set of size 3×2 modes shown in figure 10. Comparing the mean flow and its shift mode obtained from the transient forced simulations to those obtained during the start-up of the unforced flow shown in figure 5, it appears that the roles of mode and shift mode are reversed, but otherwise the spatial distribution is similar. This is to be expected, since the majority of the data in the transient forced simulations are acquired with the forcing active. Thus, more energy is contained in the modes modelling the controlled flow, making them dominant in terms of energy over the modes representing the unforced flow. The mode amplitudes shown in figure 11 confirm this; the amplitude of, for example, mode $i = 2$, $j = 1$ is larger than the amplitude of mode $i = 2$, $j = 2$ during the time when the forcing is active.

In order to minimize the number of modes as much as possible, the DPOD model was truncated to include only main modes $i \leq 3$, which contains the mean flow and the two von Kármán modes. This 3×2 mode model was then projected onto all ten of the open-loop forced simulations performed within the lock-in region indicated in figure 8, including the four simulations used for derivation and the additional simulations performed for model verification only. The mode amplitudes obtained by this projection for one of the simulations that was *not* used to derive the spatial modes are shown in figure 11. These mode amplitudes were then used to reconstruct the flow field, and the reconstructed flow field was compared to the simulation results. The modelled flow field, reconstructed from these mode amplitudes and their respective spatial modes, was then compared to the results of the numerical simulation. The instantaneous r.m.s. error of the streamwise velocity component within the entire x/D , y/D POD plane is shown in figure 12. Although the error is about 1% of the free-stream velocity during the unforced times ($t/T < 18$ and $t/T > 33$) at the beginning and end of the simulation, it is largest during the transient encountered

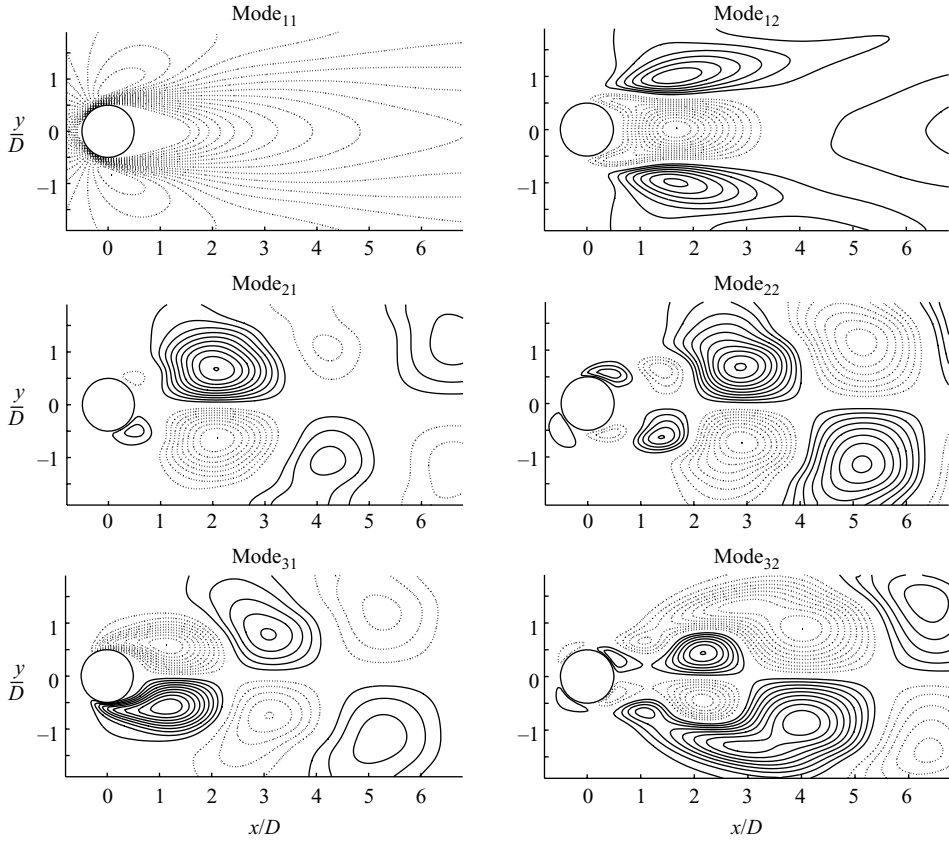


FIGURE 10. Transient forced DPOD spatial mode set using one shift mode for each main mode, the first 3×2 DPOD modes are shown. Iso-contours of streamwise velocity are shown, solid lines are positive, dashed lines negative.

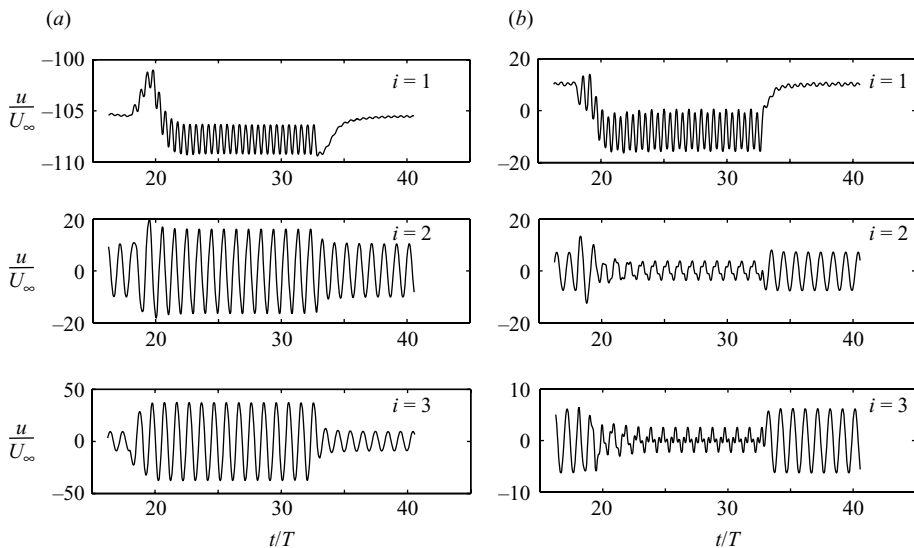


FIGURE 11. Mode amplitudes a_{ij} of the open-loop forced simulation $f/f_0 = 1$ and $A/D = 0.25$. Forcing activated at $t/T = 18$ and stopped at $t/T = 33$, after 15 full forcing cycles. The first 3×2 DPOD mode amplitudes are shown. (a) $j = 1$, (b) $j = 2$.

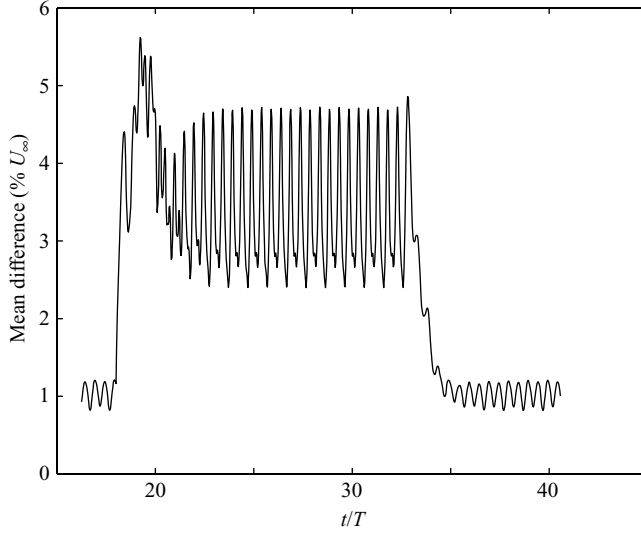


FIGURE 12. Root mean square error of the reconstructed streamwise velocity component in per cent of free-stream velocity averaged over the entire flow field. Simulation $f/f_0 = 1$ and $A/D = 0.25$. Forcing activated at $t/T = 18$ and stopped at $t/T = 33$, after 15 full forcing cycles. Mode set of 3×2 DPOD modes.

	Truncation 3×2	Truncation 5×3	Truncation 5×5	Truncation 8×7
Modes in main direction I	3	5	5	8
Modes in shift direction J	2	3	5	7
Number of modes	6	15	25	56
Estimation error (% U_∞)	3.86	1.67	1.03	0.36

TABLE 1. Root mean square error of the streamwise velocity component in per cent of free-stream velocity averaged over the entire flow field and simulation time as a function of mode truncation. The data set analysed is the transient development of the limit cycle.

after starting the forcing, with a second smaller peak when the forcing is turned off. During the phase-locked portion of the simulation ($t/T = 22 \dots 33$) the error is about 4% of the free-stream velocity, or four times larger than in the unforced case.

There are two main reasons for this increase: (i) since this particular data set was not used for the development of the spatial modes, the match of the spatial modes to the data is less than optimal; and (ii) the open-loop forcing creates larger amplitudes of higher-frequency disturbances, as can be seen by inspecting the fluctuation amplitudes in the error during the unforced and locked-in portions of the simulation. During the lock-in portion, these fluctuations are significantly larger, indicating more energy in the higher-order modes. Since these modes have been truncated, however, the error increases owing to spill-over effects. Overall, however, the modelling error never exceeds 6% of the free-stream velocity, and is usually well below 5%. This is more than sufficient for typical feedback-control purposes. Furthermore, the error may be reduced by retaining more modes using less aggressive truncation of the model. This is shown in table 1, where the same DPOD model is truncated to different numbers

Case number	Forcing frequency (100 % f_0)	Forcing amplitude (y/D)	Time-averaged mean flow field difference ($\%U_\infty$)
1	1	0.25	2.65
2	1	0.3	3.00
3	1.05	0.3	2.97
4	0.9	0.3	2.97
5	1.1	0.3	3.18
6	0.95	0.3	2.91
7	1	0.2	2.38
8	1	0.1	1.79
9	1	0.15	2.09

TABLE 2. Time-averaged r.m.s. errors of the streamwise velocity component in per cent of free-stream velocity averaged over the POD domain and simulation time for all different transient forced simulations using the DPOD modes truncated to 5×3 modes.

of main and shift modes. From an actual comparison between the original CFD data and the truncated DPOD estimates, it can be seen that the estimation error becomes smaller as the number of modes retained in the model is increased. This decrease in error is consistent with the roll off seen in the mode energy plot (figure 6). Although only one particular data set, the forcing using 25 % of the cylinder diameter displacement at the natural shedding frequency, is presented for reasons of brevity, all investigated data sets show errors over time similar to that presented in figure 12.

The time averaged r.m.s. errors for all different data sets are summarized in table 2. These results are based on a 6 mode model consisting of modes 11 to 32 shown in figure 10. These same modes were projected onto all data sets in the same fashion as presented for the forcing case $A/D=0.25$, $f/f_0=1$ in order to determine the errors shown in table 2. Although we expect to find larger errors for data sets not used for spatial mode development, the error magnitude correlates more with forcing amplitude than anything else. This is another indication that modal truncation drives the error. For larger forcing amplitudes, more energy is contained in the truncated higher-order modes. With the largest error at 3.18 %, however, the agreement between the model and the flow field can be considered to be quite good. This agreement is a necessary prerequisite for the development of a low-dimensional mathematical model based on the mode amplitudes which will be described in the following chapter.

In summary, DPOD is a computational tool that is suitable for developing low-dimensional POD bases that span a variety of flow conditions, both from different Reynolds numbers and different forcing inputs. Additionally, transient flow situations can be modelled with good accuracy. The resulting DPOD basis is also valid for flow situations that were not included in its derivation, as long as they are within the parameter range spanned by the snapshots used for derivation of the basis, which constitutes an interpolation capability of the DPOD basis.

5. Low-dimensional modelling of DPOD mode amplitudes

With the DPOD spatial mode basis, developed in the previous section, covering a range of both Reynolds numbers and forcing conditions, the entire time-dependent global dynamic behaviour of the flow is captured in the corresponding mode amplitudes. Thus, the next goal is to develop a set of equations describing the dynamic behaviour of these mode amplitudes. These equations are required both for

development of control algorithms, and for testing these controllers. Traditionally, Galerkin projections of various types have been used to project the mode amplitudes onto the Navier–Stokes equations. However, this approach has led to a variety of problems which are discussed in §§1 and 5.1, leading us to use a different modelling approach as described in the following section.

5.1. *General comments on the modelling approach*

Before initiating the description of the development of a meaningful low-dimensional model of the DPOD mode amplitudes, it is advisable to determine the characteristics most sought after, and the corresponding choices made in this effort. Given the complexity of the problem at hand, it may not be possible to address it with an off-the-shelf package, but instead with a unique synthesis of a few tools that appear to be promising. The most important features are as follows.

5.1.1. *Structured scalable methodology*

Developing an *ad hoc* approach, as demonstrated by Gillies (1995) using the least-squares technique, may address a particular problem for a given design point under certain conditions, but is not generic enough. We would like an approach which may be applied to a wide range of flow conditions (e.g. Reynolds numbers). Another important principle is to let the data determine the dynamic complexity, i.e. the number of DPOD modes of the reduced-order model, using defensible criteria. This approach differs from that of Noack, Tadmor & Morzynski (2004a), who use first principles to make an *a priori* decision on the number and nature of the modes.

5.1.2. *Numerical issues and model stability*

The nonlinearity and scaling characteristics of the modes lead to numerical stability issues which undermine the development and analysis of effective estimation and control laws. In certain instances, numerical problems arise owing to the effects of noisy data on the computation of higher-order derivatives. This may be resolved, as shown by Deane *et al.* (1991), where only first derivatives are used by transforming the viscous term using Green’s law. In an alternative approach to assuring model stability, the ARX (Auto Regressive eXternal input) dynamic model structure, which is widely used in system identification, is incorporated. A salient feature of the ARX predictor is that it is inherently stable even if the dynamic system to be modelled is unstable. This characteristic of ARX models often lends itself to successful modelling of unstable processes (Nelles 2001).

5.1.3. *Model validity and robustness*

A prerequisite of model building is the determination of the dynamic envelope within which the model is valid. Later, after obtaining a reduced-order model, we must ensure that it is capable of providing relatively accurate predictions within this desired validity region, as described by the envelope presented in figure 8. In a following section, we demonstrate the ability of the model to predict the flow field when provided with a complex input signal obtained from a closed-loop CFD simulation.

5.1.4. *Universal approximation of nonlinear mappings*

It would be desirable to obtain a linear model that is able to meet all of the requirements described above. Unfortunately, limitations in the ability of linear systems to model a nonlinearly saturated limit cycle oscillation are to be expected. However, in some instances, certain nonlinear systems may be successfully modelled

using the addition of a set of virtual states (Ljung 1999). We spent some considerable time in vain trying to apply state-of-the-art structured numerically stable system-identification techniques to this flow field. Linear state-space models having 25–90 states were developed and we concluded that the predictive capability is insufficient for feedback control as detailed by Cohen *et al.* (2006). Consequently, we decided to look into universal nonlinear approximators, such as artificial neural networks (ANNs), for their inherent robustness and capability to approximate any nonlinear function to any arbitrary degree of accuracy (Cybenko 1989). The ANN employed in this effort, in conjunction with the ARX model, is the mechanism with which the dynamic model is developed using the DPOD mode amplitudes obtained from the CFD simulation data. Nonlinear optimization techniques, based on the back-propagation method, are used to minimize the difference between the DPOD mode amplitudes and the ANN-ARX model estimation of the same while adjusting the weights of the model (Haykin 1999). While ANNs have many advantages as stated, there are also drawbacks. These, however, can be avoided by proper design and analysis approaches, as described in the following. The input–output set must be carefully constructed so as to avoid problems such as numerical ill-conditioning, over-fitting the data during the learning stage, and ensuring that the data is not over-represented in one region in comparison to another region (Nørgaard *et al.* 2000). A major problem using ANNs concerns stability analysis. One of the best methods to address this is a stochastic robustness analysis technique based on Monte Carlo simulations. This approach, while more time-consuming than stability analysis for linear models, is more accurate than using linearized stability methods, since it does not make any simplifying assumptions. However, this added numerical effort is small compared to the numerical cost of the CFD simulations.

5.2. Mathematical formulation of the ANN-ARX method

System identification of a cylinder wake can be accomplished with a linear ARX model,

$$a(t) = q^{-d} \frac{\mathbf{B}(q^{-1})}{\mathbf{D}(q^{-1})} f(t) + \frac{1}{\mathbf{D}(q^{-1})} e(t), \quad (5.1)$$

where $a(t)$ is the state vector representing the POD mode amplitudes $a_j(t)$ shown in (1.1). $f(t)$ describes the external input, which in the current effort is the vertical displacement of the cylinder and $e(t)$ is the white noise vector. For the above case, \mathbf{B} and \mathbf{D} are matrix polynomials in q^{-1} .

The time delay operator is defined as

$$q^{-d} a(t) = a(t - d), \quad (5.2)$$

where d is a multiple of the sampling period. The parameter matrix, θ , and the regression vector, $\phi(t)$, are respectively defined as

$$\theta = [d_{ij} b_{ij}]^T, \quad (5.3)$$

$$\phi(t) = [a(t - 1), \dots, a(t - n), f(t - d), \dots, f(t - d - m)]^T. \quad (5.4)$$

As can be seen in (5.4), the vector $\phi(t)$ is comprised of past states and past inputs.

The ARX predictor (Ljung 1999) may then be written as

$$\hat{a}(t|\theta) = q^{-d} \mathbf{B}(q^{-1}) f(t) + [1 - \mathbf{D}(q^{-1})] a(t) = \varphi^T(t) \theta. \quad (5.5)$$

Equation (5.5) represents an algebraic relationship between the prediction, given on the left-hand side, and past inputs and states, summarized by $\phi(t)$. The parameter

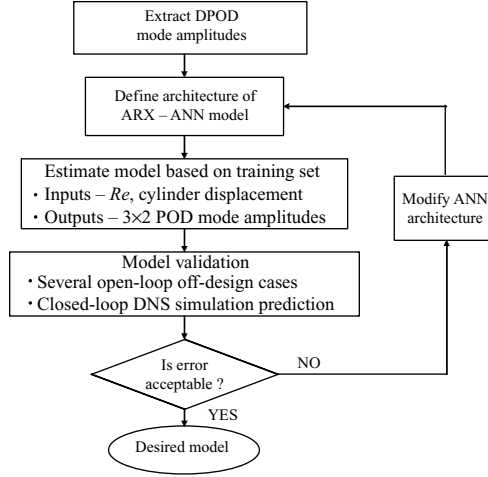


FIGURE 13. System identification for dynamic modelling of DPOD mode amplitudes.

matrix, θ , is determined during the estimation process. The main advantage of the ARX predictor is that it is always stable, even when the dynamic plant (the flow field in this case) being estimated is unstable. This feature is of utmost importance when modelling an unstable system such as the absolutely unstable cylinder wake flow.

The main drawback of this approach is that it is limited to modelling of linear systems which, as described above, is insufficient for modelling of unstable limit cycles. A general representation of nonlinear system identification, based on a hybrid ANN-ARX approach (Nørgaard *et al.* 2000), may be written as

$$a(t|\theta) = g[\varphi(t), \theta] + e(t), \quad (5.6)$$

where θ is the matrix containing the weights of the ANN that are estimated by a back-propagation algorithm using a training data set (Nørgaard *et al.* 2000), and g is the nonlinear mapping realized by the feed-forward structure of the ANN.

The ANN-ARX predictor can then be expressed as

$$\hat{a}(t|\theta) = g[\varphi(t), \theta]. \quad (5.7)$$

The basic methodology to design an ARX-ANN plant for dynamic modelling of the DPOD mode amplitudes is presented in figure 13. The ANN-ARX algorithms used in this effort are a modification of the toolbox developed by Nørgaard *et al.* (2000). We performed three main modifications to the toolbox. The first extends the toolbox for use in simulations, as opposed to one-step prediction, of MIMO (multi-input, multi-output) systems. Secondly, the implementation of the *time tapped delay* system allows for the periodic sampling rate of inputs to the network. This helps to decrease network training times, and also extends the time history of the inputs while keeping the number of inputs low. Thirdly, the network was decoupled, meaning the modes could be trained separately and compiled into one large network at the end. This allowed for greater flexibility in training each individual mode. Although this resulted in a much larger, more complex final network, simulation times are negligible when compared to training times. A schematic representation of the feed-forward ANN-ARX network topology is presented in figure 14. After the DPOD mode amplitudes were obtained from the CFD data as described in the previous section, a single hidden layer ANN-ARX architecture was selected. The training set comprised input-output

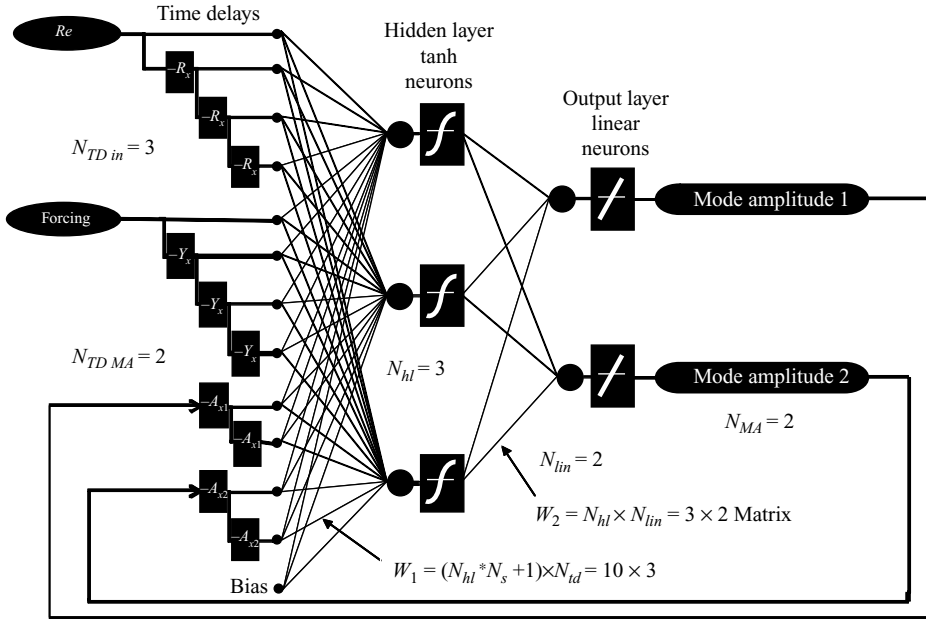


FIGURE 14. Example ANN-ARX system identification network topology. The model displays a two-layer (tanh and linear), 3 neuron, 2 mode output, 12 input neural network. The periodic sampling rates R_x , Y_x , A_{xn} , account for the number of time delays between sampled data points. Refer to table 3 for actual time delays and number of inputs for the 2×3 DPOD-ANN-ARX model.

data obtained from CFD simulations. The model is validated for off-design cases and if the estimation error is unacceptable, then the ANN architecture is modified. This cycle was repeated until estimation errors were acceptable for all off-design cases.

The ANN-ARX predictor is inherently stable because, although the modelling approach is nonlinear, the algebraic relationship between the prediction and past states and inputs is preserved. This is extremely important when dealing with nonlinear systems represented by PDEs such as the Navier–Stokes equations, since the stability problems are more severe than in linear systems. The ANN-ARX approach is an ideal choice when the system to be modelled is deterministic and the signal to noise ratio (SNR) of the data is good (Nørgaard *et al.* 2000).

The choice of the specific artificial neural network (ANN) architecture was based on three main design criteria. The first concerns the number of hidden layers. This was selected as one, i.e. a single hidden layer, since it is the simplest form that allows for a universal approximator (Cybenko 1989) and its effectiveness for system identification problems has been shown by Nørgaard *et al.* (2000). The second decision concerns the number of nodes. If the number of nodes in the hidden layer is small, the resulting error is unacceptable. As the number of nodes is increased, the error is reduced at the expense of computational complexity until a number of nodes is reached beyond which no further improvement in error is observed. The third design criterion is the choice of the network input’s time histories and delays. Larger sampling periods (more data inputs) allow for a more dynamically based network. Networks with larger time histories are more accurate because of their ability to predict future outputs based on a better knowledge of the past. The trade-off is that training time is greatly increased with larger input vectors. The time tapped delay technique allows for a much broader

Input	Number of past inputs or outputs to neural net	Delay between inputs	Total time history
Reynolds number	1	R_x	10
Actuator position	4	Y_x	8
Mode 1,1	1	$A_{x1,1}$	1
Mode 2,1	3	$A_{x2,1}$	24
Mode 3,1	3	$A_{x3,1}$	24
Mode 1,2	1	$A_{x1,2}$	1
Mode 2,2	1	$A_{x2,2}$	12
Mode 3,2	1	$A_{x3,2}$	12

TABLE 3. Network topology representing inputs and their time delays of the 3×2 DPOD-ANN-ARX model. The number of past inputs per signal and the delay which is the number of time steps in between sampling periods (R_x , Y_x , A_{xn}) are shown. The product of these two is the total time history.

sampling period while keeping the number of inputs low, thus improving the training speed. For example, instead of using every single past delay input for a certain period of time, the time tapped delay can be set to 2 and the network will skip every other data point, thus reducing the number of inputs by 50% while maintaining the same total length of the sampling history. The time tapped delays for the Reynolds number input (R_x), actuator input (Y_x) and previous mode amplitudes (A_{xn}) are presented in table 3. Figure 14 represents a simple example of an ANN-ARX model.

Initially, neural networks were designed and trained for the 6 mode (3×2 DPOD) model. However, training times were excessive, leading to the realization that new techniques were necessary. The network was split into smaller sub-networks which could be trained much more efficiently. These smaller networks can be superimposed and compiled into a larger overall network. Thus, many parameters exist in the design of ANN-ARX models. The resulting ANN has the following features.

Input layer. There are two network input parameters, the normalized cylinder displacement and the Reynolds number. In addition to these readings, in order to obtain a strong representation of the dynamics of the system, the input layer includes past outputs of the six modes and past inputs for each of the two inputs (Reynolds number and cylinder displacement) as described in the toolbox developed by Nørgaard *et al.* (2000). Table 3 presents the actual input/output time delays. The number of time delays for the past outputs was about one shedding cycle. On the other hand, the number of time delays for the past inputs was about half a shedding cycle. The selection of time delays for past inputs/outputs was based on a sensitivity study which investigated the trade-off between estimation accuracy and network complexity. Therefore, the final configuration of the input layer chosen includes six mode outputs, namely, the first three main DPOD modes $i=1, j=1$; $i=2, j=1$; $i=3, j=1$ and their shift modes with a maximum of 24 time delays; two inputs, the Reynolds number and the actuator position for a maximum of 10 time delays; and one bias input. The total number of inputs to the net is therefore 15 (see table 3).

Hidden layer. There is one hidden layer consisting of 130 neurons. The activation function in the hidden layer neurons is the tanh function. A single bias input has been added to the output from the hidden layer.

Output layer. There are 6 outputs, namely, the 6 states representing the DPOD mode amplitudes of the 3×2 DPOD spatial mode basis. The output neurons have linear activation functions.

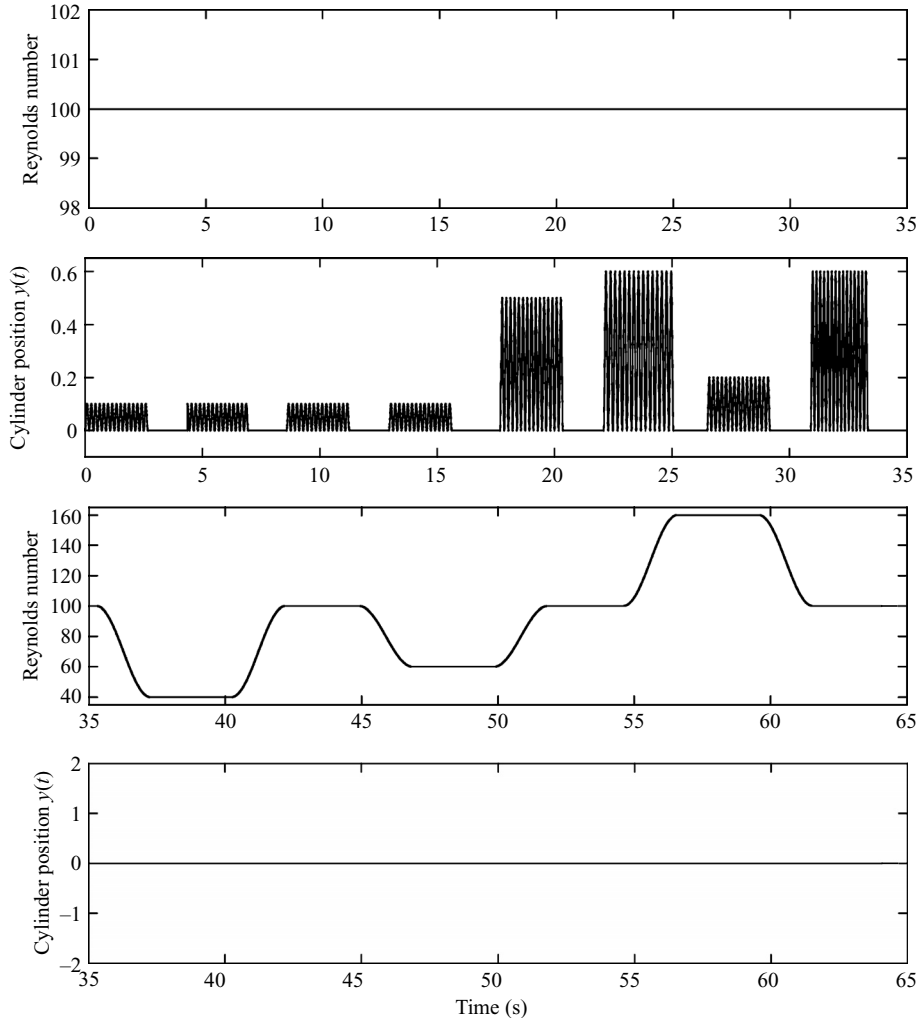


FIGURE 15. Neural network training data. $t=0$ s to 35 s: cylinder displacement: Case 10 at 4 different phase angles of 0° , 90° , 180° and 270° , Case 1, Case 4, Case 5, Case 8 (see figure 8). $t=35$ s to 64 s: Reynolds number transients: $100 \rightarrow 40 \rightarrow 100 \rightarrow 60 \rightarrow 100 \rightarrow 160 \rightarrow 100$.

Weighing matrices. The weighing matrix between the input layer and the hidden layer is of size (130×16) , whereas the weighing matrix between the hidden layer and the output layer is of size (6×131) . These weighing matrices are initialized randomly before training.

Training the ANN. Back propagation, based on the Levenberg–Marquardt algorithm, was used to train the ANN using the toolbox of Nørgaard *et al.* (2000). The training data (21 790 time steps) is comprised of output from multiple CFD simulations (figure 15). The first portion of the training consists of open-loop forced transient simulations comprising design cases 1, 4, 5, 8, 10 (see figure 8). The forcing of case 10 is repeated four times, with different starting phase angles of 0° , 90° , 180° and 270° between the shedding of the vortices in the wake and the actuation signal at the start of the actuation. This leads to very different transient adjustment in the wake, which was found to be an essential feature for network training. During these

Mode i, j	Case 1	Case 4	Case 5	Case 8	Case 10	Case 2	Case 3	Case 6	Case 7	Case 9
Design case:	Yes	Yes	Yes	Yes	Yes	No	No	No	No	No
1,1	0.7%	0.1%	0.2%	1.0%	0.0%	0.4%	0.7%	0.6%	2.0%	2.2%
2,1	2.4%	2.6%	4.2%	1.9%	0.1%	2.0%	3.8%	2.5%	0.6%	1.6%
3,1	3.8%	5.9%	0.9%	2.1%	0.4%	1.5%	1.2%	1.7%	2.2%	1.6%
1,2	5.5%	1.8%	2.3%	49.8%	49.1%	7.8%	10.5%	5.5%	52.4%	9.5%
2,2	1.1%	10.7%	0.6%	4.0%	4.5%	7.7%	7.8%	9.2%	7.3%	9.8%
3,2	2.9%	16.9%	24.0%	9.1%	36.4%	7.3%	28.1%	8.4%	0.6%	19.7%

TABLE 4. Relative r.m.s. errors in per cent of the mean mode amplitude a_{ij} for DPOD-ANN-ARX estimated mode amplitudes compared to the DPOD mode amplitudes obtained from CFD simulation. The DPOD model is truncated to 3×2 modes for both model and CFD results.

open-loop actuation simulations, the Reynolds number is fixed at $Re = 100$. The second portion of the training data set is comprised of transients in Reynolds number, while the actuation is kept at zero level. The Reynolds number transient training data include ramping from $Re = 100$ to 40, from $Re = 100$ to 60 and from $Re = 100$ to 160. These two data sets were concatenated into one hybrid dataset, presented in figure 15. Along with the 3×2 DPOD mode amplitudes, the Reynolds number as well as the cylinder displacement were provided as inputs to the network. The training procedure converged after 50 to 150 iterations depending on which mode was being trained. The comparison between original mode amplitudes and mode amplitudes as estimated by the model is illustrated in figure 18(a). For the 3×2 mode amplitudes, the percentage estimation error, computed as $e = [(RMS_{Actual} - RMS_{Simulated})/RMS_{Actual}] \times 100$, is presented in table 4. This error definition emphasizes the amplitude error which is the key parameter for the model to be useful for controller development. It can be seen that the training data is represented very well by the model (first 5 columns of table 4), which should not be surprising because nonlinear function approximation is the very strength of the back-propagation training algorithm. In the next section, we investigate the validity of the model for off-design cases, which is the true test of usefulness of the ANN for feedback flow control.

6. Simulation of open-loop and feedback-controlled computations using the ANN low-dimensional model

The nonlinear ANN-ARX model was developed using five design cases (Cases 1, 4, 5, 8 and 10) for training of the ANN within the lock-in region. Five simulations not used for model development (2, 3, 6, 7 and 9), shown in figure 8, were used for validation of the model. The percentage RMS error of the mode amplitude, for the 3×2 modes, is presented in table 4. Each case is comprised of 1500 time steps. As seen in table 4, the validation of the ANN for five different cases within the lock-in region provided promising results and shows accuracy as well as stability and robustness.

Figure 18(a) shows the CFD based DPOD mode amplitudes in comparison to the ANN-ARX model estimates for design case 1 and figure 18(b) shows one of the off-design cases (3). Note the accurate estimation of the mode amplitudes by the ANN-ARX model when the forcing is switched on and off in a transient fashion. Although we present only one off-design case, the other cases are qualitatively and quantitatively similar to case 3 in figure 18(b). As reported by Cohen *et al.* (2006), attempts made

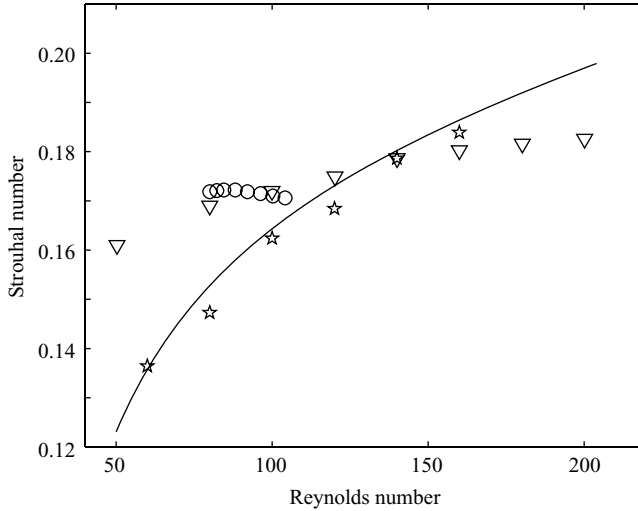


FIGURE 16. Comparison of ANN-ARX model of unforced vortex shedding at different Reynolds numbers to experimental data and models developed by Noack *et al.* (2003). Solid line, curve fit of experimental data described by $St = -3.3265/Re + 0.1816 + 1.6 \times 10^{-4} Re$ presented in Williamson (1996). *, ANN-ARX model; ▽, model A presented in Noack *et al.* figure 12(a). ○, model B presented in Noack *et al.* figure 12(a).

at modelling these transients with a linear system identification approach were not nearly as successful.

Another important model property is robustness against changes in operating conditions, in our case, the Reynolds number. While the main goal of model development and training was to obtain a model that accurately represents the flow changes due to forcing, it is important that the model delivers accurate results in the vicinity of the design point with respect to Reynolds number. The ANN-ARX model was also validated for the start up transient behaviour of the shedding cycles. Figure 17 clearly shows the similarity between a CFD simulation and ANN-ARX model estimation when increasing the Reynolds number from 40 to 100. We also ran unforced (actuation amplitude $A/D = 0$) ANN-ARX simulations at different Reynolds numbers between 60 and 160 and computed the shedding frequency obtained from the model and converted them to the Strouhal Number. The results are presented in figure 16 in comparison to a curve fit to experimental data presented by Williamson (1996). While not shown, all of the simulations at different Reynolds numbers developed stable limit cycles with no divergence of the mode amplitudes over time, demonstrating the long-term stability of the model. The ANN-ARX results show good agreement with experimental data, even though training of the model was by no means optimized to obtain accurate results at different Reynolds numbers. This could be improved upon by adding more transient Reynolds-number data to the training data ensemble. Also shown in comparison are Galerkin-model results presented by Noack *et al.* (2003), obtained with the best published model for the circular cylinder wake at a Reynolds number of 100, according to our best knowledge. Their models A and B, which use eight POD modes and eight POD modes plus a shift mode, respectively, were obtained using a Galerkin projection of the mode amplitudes onto the Navier–Stokes equations. Model A is equivalent to the benchmark model by Deane *et al.* (1991), while model B includes the shift mode developed from the steady

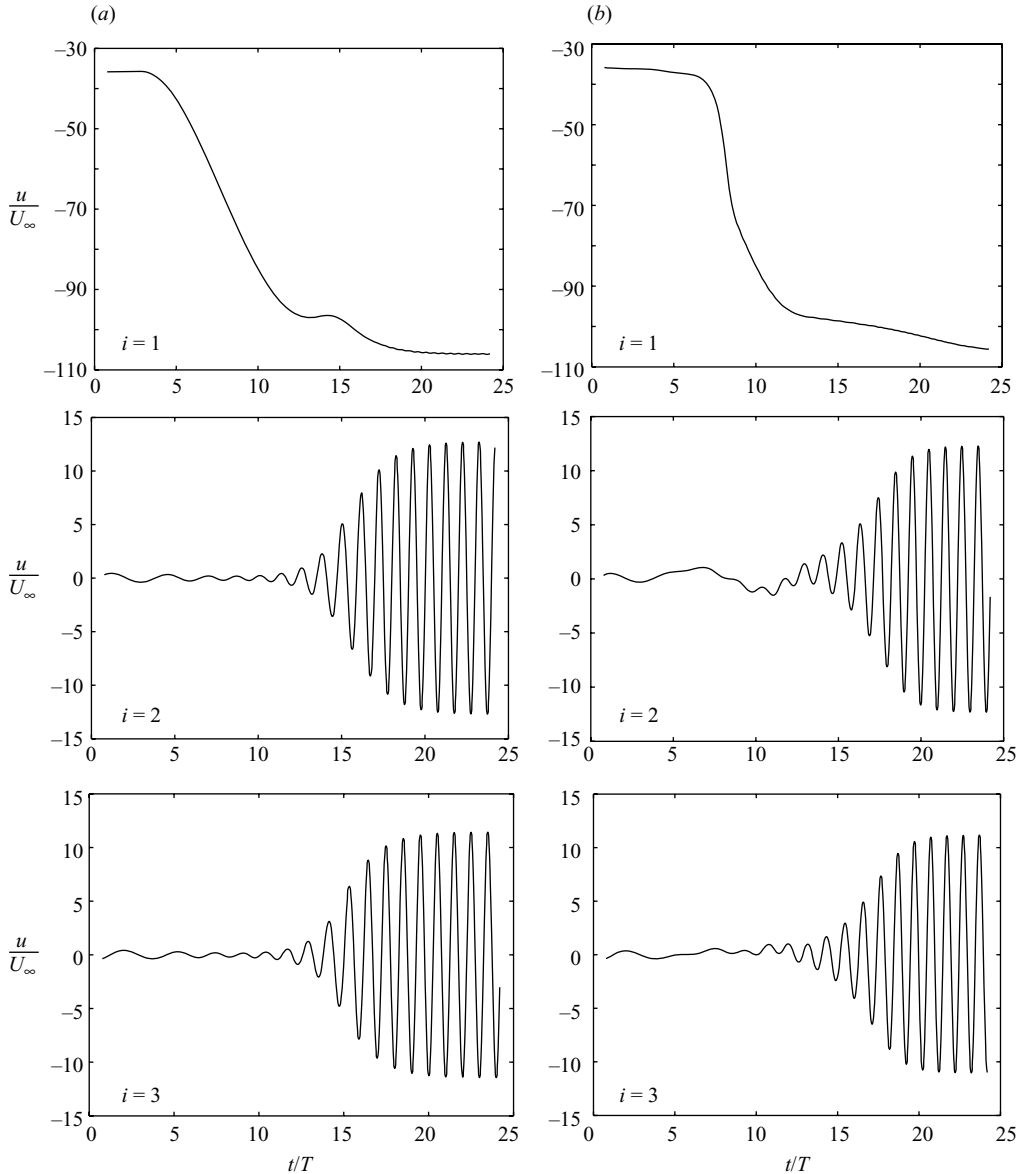


FIGURE 17. Mode amplitude comparison between CFD simulation and ANN-ARX model for Reynolds number transients from $Re = 40$ to 100 of the modes 1,1; 2,1 and 3,1. (a) CFD simulation, (b) ANN-ARX model simulation. $j = 1$.

solution of the flow field. It can be seen that the ability of both models A and B to capture correctly the natural shedding frequency at off-design Reynolds numbers falls short of the performance of the ANN-ARX-DPOD model developed in this work.

In addition to the open-loop forced validation cases and the off-design Reynolds number studies presented above, a closed-loop simulation result was used to test the DPOD-ANN-ARX model's ability to estimate feedback-controlled cylinder wake flows. These results have been presented by Siegel, Cohen & McLaughlin (2006). Figure 19 shows the pertinent results of this CFD simulation in terms of mode amplitudes, lift, drag and controller phase. The feedback control law was a PD controller with

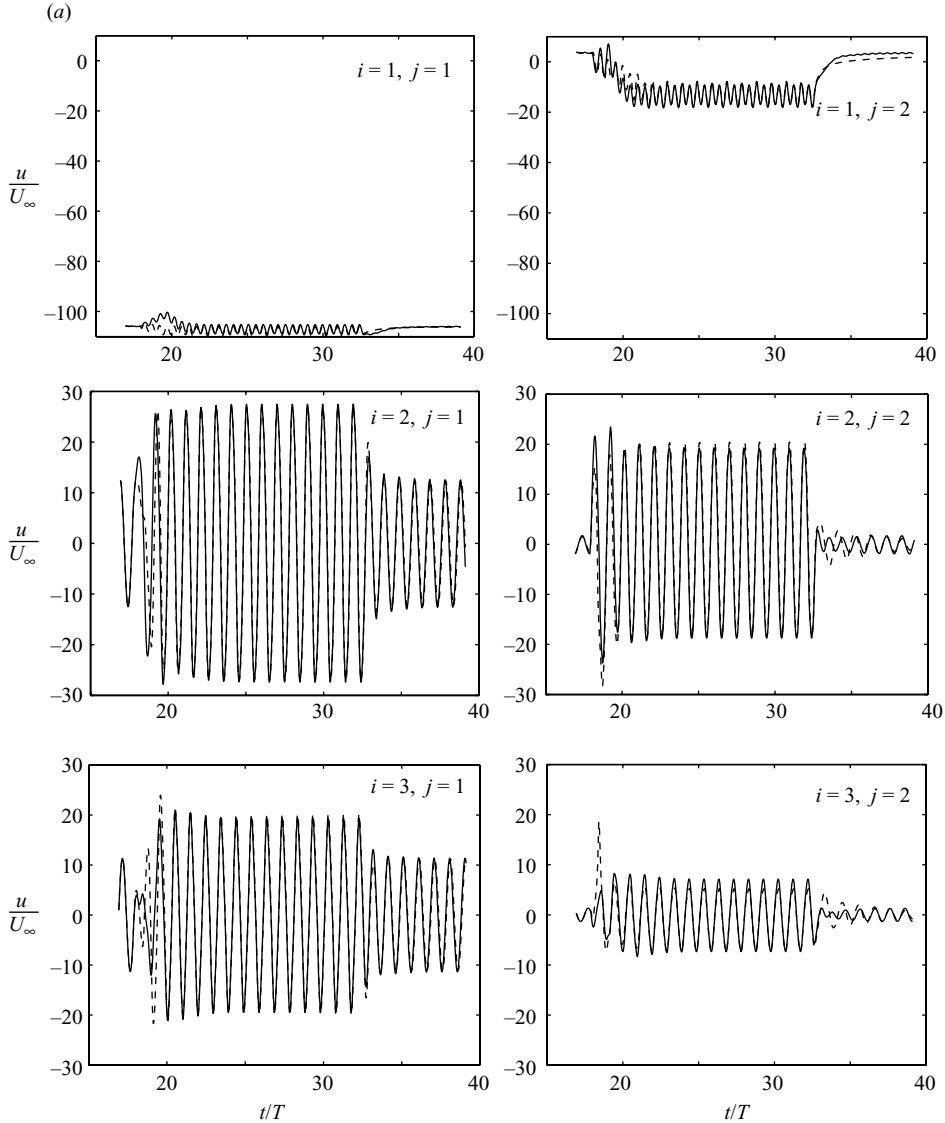


FIGURE 18(a). For caption see next page.

adjustable gains. For all investigations, only displacement of the cylinder in the flow normal direction was employed for forcing the flow. The control algorithm acts on amplitude estimates of POD modes, where the POD model in this investigation included four main modes and a shift mode. These modes are qualitatively similar to modes $i = 1, j = 1 - i = 4, j = 1$ and the shift mode is similar to mode $i = 1, j = 2$ as shown in figure 10. This design decision was made based on our earlier investigations controlling a low-dimensional model of the flow (Cohen *et al.* 2003). For the low-dimensional model, proportional gain applied to the first von Kármán mode was sufficient to suppress vortex shedding. The employed PD feedback control strategy can be written as

$$y_{cyl} = K_p a_{21} + K_d \frac{da_{21}}{dt}. \quad (6.1)$$

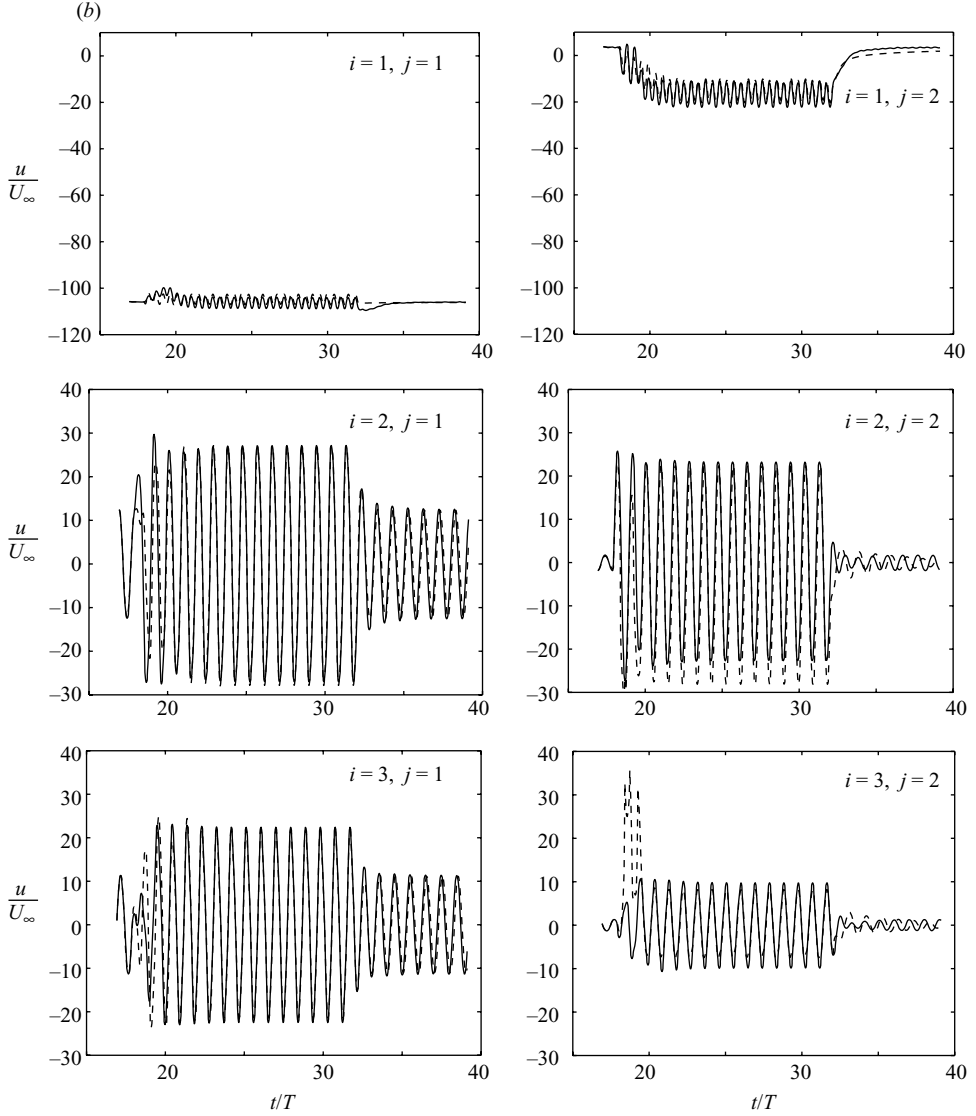


FIGURE 18. (a) Mode amplitudes a_{ij} of the first 3×2 DPOD modes for one of the design cases, forcing with $f/f_0 = 1$ and $A/D = 0.25$. This data was used for training of the ANN-ARX network. (b) Mode amplitudes a_{ij} of the first 6 DPOD modes for the off-design case 3, forcing with $f/f_0 = 105$ and $A/D = 0.30$. This data was not used for training of the ANN-ARX network. Lines, mode amplitudes from the CFD simulation; dot-dash lines, mode amplitude estimation from the ANN-ARX model.

Instead of directly specifying the K_p and K_d gains, they can be expressed in terms of an overall gain K and a phase advance φ ,

$$K_p = K \cos(\varphi), \quad (6.2a)$$

$$K_d = \frac{K \sin(\varphi)}{2\pi f}, \quad (6.2b)$$

where f is the natural vortex-shedding frequency.

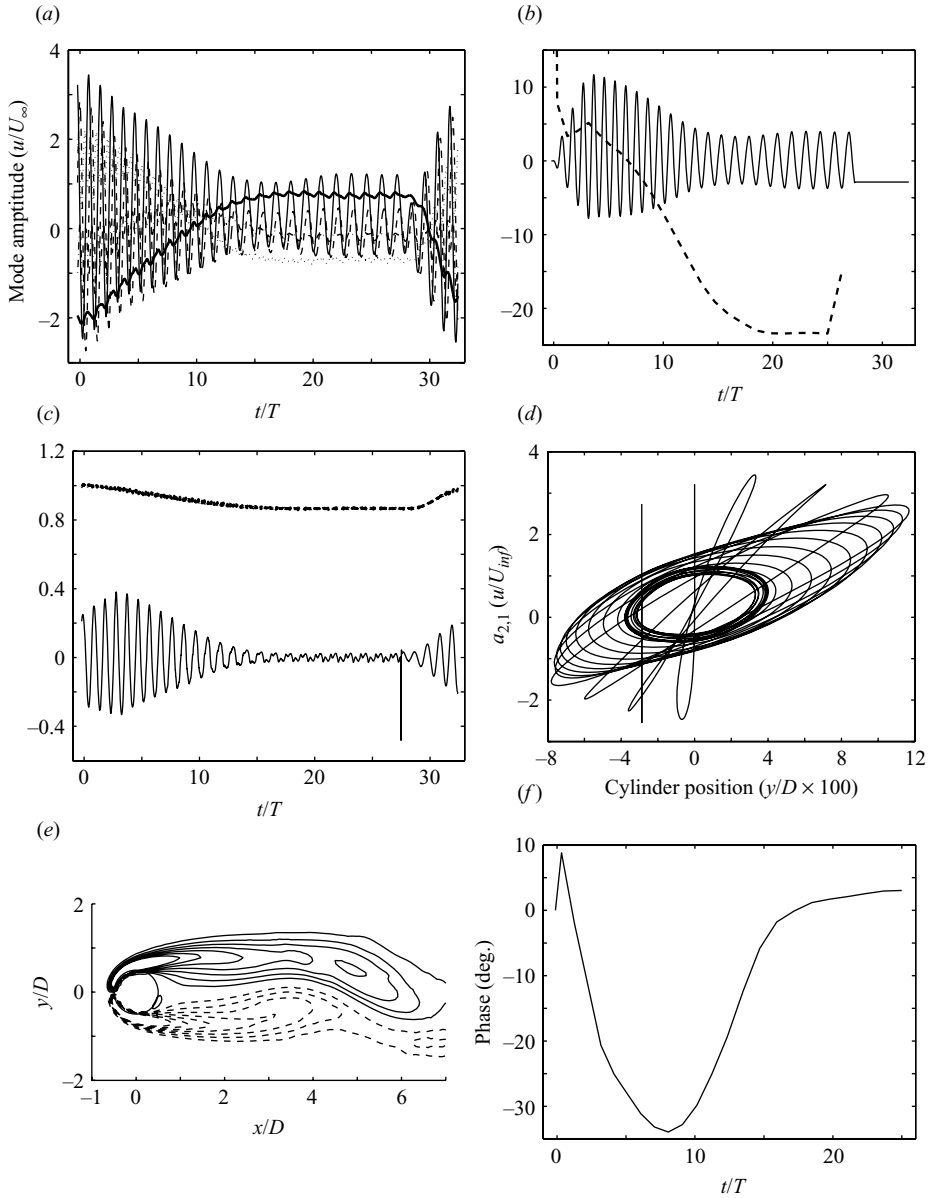


FIGURE 19. Linear feedback of mode amplitude a_{21} with a linear proportional-differential variable gain controller as presented in Siegel *et al.* (2006). $K_0 = 1 \times 10^{-3}$, $\varphi = 15^\circ$, $K_A = 1 \times 10^{-6}$, $K_j = 0.75^\circ$. (a) Mode amplitudes; a_{21} (—), a_{31} (---), a_{41} (⋯), a_{51} (·-·), a_{12} (- -). (b) Cylinder displacement $y/D \times 100$ (-) and frequency $(f - f_0)/f_0$ (- -). (c) Non-dimensional lift (thin line) L/D_0 , and drag (thick line) D/D_0 forces. (d) Phase between cylinder position y and a_{21} . (e) Instantaneous vorticity contours at $t/T = 24.7$. (f) Phase advance during the run. The controller is activated at $t/T = 0$ and deactivated at $t/T = 27.5$.

During the course of the investigations, we found it advantageous to implement a variable gain strategy. The basic idea is that as the flow field is modified from its original state, different values for the phase advance φ and the gain K may be more advantageous than those effective in controlling the unforced flow field. Using the

amplitude difference between the unforced state and the current state, K and φ are written as

$$K = K_0 + K_A(a_{12} - a_{12}|_{t=0}), \quad (6.3a)$$

$$\varphi = \varphi_0 + K_\varphi(a_{12} - a_{12}|_{t=0}). \quad (6.3a)$$

Equation (6.3) details the adjustment scheme for the variable gain strategy. Since mode 12 is a good measure of the change in the mean flow, the feedback gain K and the phase advance φ are adjusted from their initial values K_0 and φ_0 in proportion to the change in mode $i=1, j=2$ by applying a phase advance factor K_φ and a gain change factor K_A . These additional factors can be either applied together or individually.

Figure 19, reproduced from Siegel *et al.* (2006), shows that a drag reduction of about 15 % of the total drag was achieved, as well as a lowering of the unsteady lift force by more than 90 %. The controller employed by Siegel *et al.* (2006) was empirical in nature, and while model-based estimation of the flow state was a crucial enabling technology, the adjustment of the linear proportional and differential feedback gains was based on trial and error rather than on a model-based flow analysis. Nonetheless, this simulation provides an excellent test case to investigate the use of the low-dimensional model developed in this work for controller development and testing. In terms of the DPOD mode amplitudes shown in figure 20(a), it can be seen that the feedback controller leads to a significant reduction of the fluctuations in the main modes $i=2, j=1$ and $i=3, j=1$. Modes $i=1, j=1$ and $i=1, j=2$ both increase in amplitude while feedback control is applied, which is consistent with a reduction in drag. The shift modes $i=2, j=2$ and $i=3, j=2$, however, show an increase in fluctuation amplitude, which indicates that the vortex-shedding activity further downstream, which is represented by these modes, has increased in intensity. One of the main difficulties in reproducing this simulation using an ANN-ARX model is due to the use of sensor-based mode estimates in the CFD simulations, which are not available in identical form from the ANN-ARX model simulation. For this reason, gains for a new PID controller were empirically developed to use the mode $i=2, j=1$ amplitude directly available from the ANN-ARX simulation for feedback. This leads to slightly different control gains, but the mode amplitudes obtained from the ANN-ARX model shown in figure 20(b) were very similar to those of the CFD closed-loop simulation shown in figure 20(a). The ANN-ARX results show similar decreases in the fluctuating main modes $i=2, j=1$ and $i=3, j=1$, while the shift modes of these modes show an increase in fluctuation intensity just as in the CFD simulations. The PID controller used for the ANN-ARX model operates on the linear combination of three terms: the proportional term, integral term and derivative term which can be written as:

$$y(t) = K_p a_{21} + K_d \frac{d a_{21}}{dt} + K_I \int a_{21} dt. \quad (6.4)$$

The gains for the ANN-ARX PID controller were determined to be $K_p = -0.45$, $K_d = -2$, $K_I = -0.1$. Figure 21 shows the output of the PID controller which is directly related to the cylinder position. Although only open-loop and transient start-up data were used for model development, the model-based estimation of the impact of feedback control on the flow of this closed-loop simulation is fairly accurate. This result demonstrates that the DPOD-ANN-ARX model captures the flow physics correctly, enabling both systematic controller development and performance evaluation.

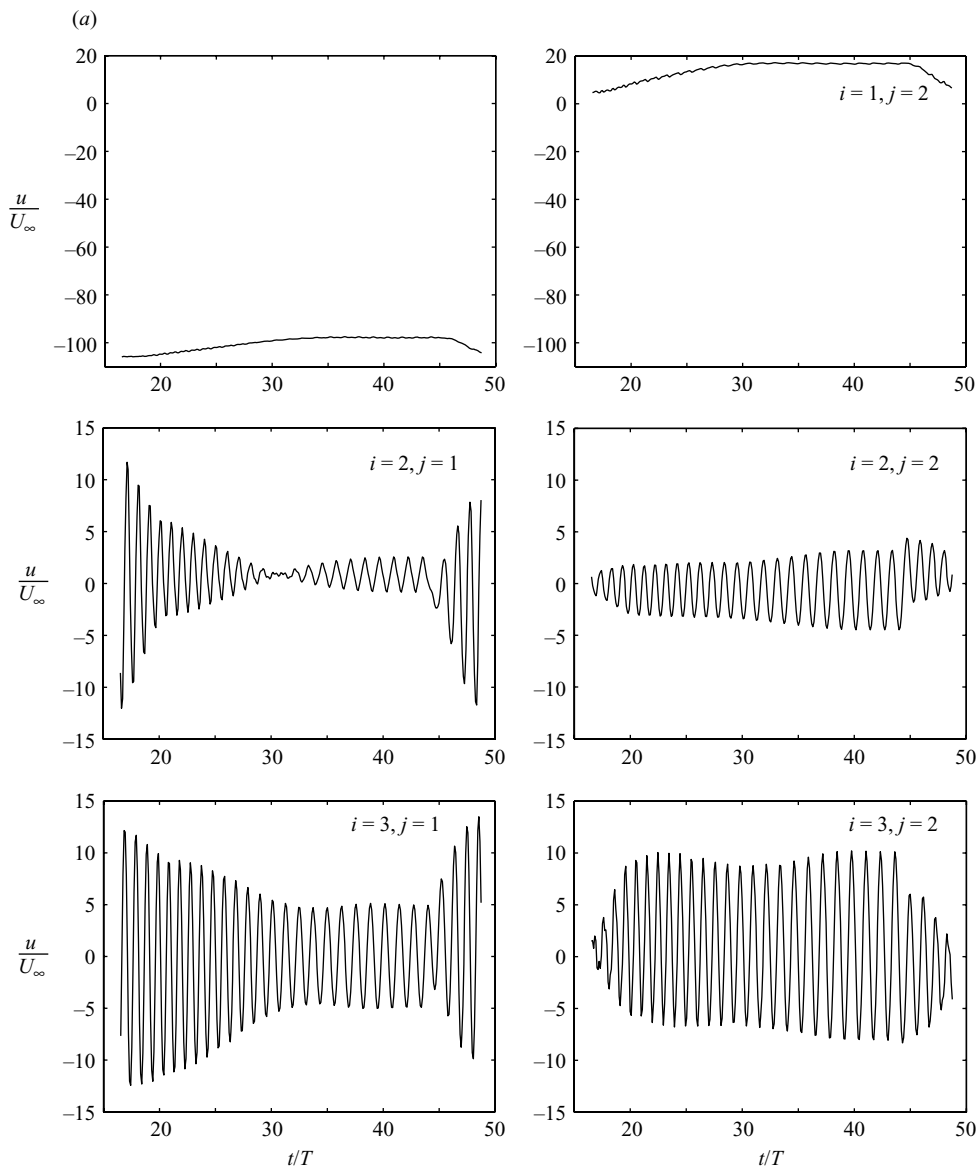


FIGURE 20(a). For caption see next page.

7. Conclusions

One of the big challenges in feedback flow control is the development of robust, numerically stable low-dimensional models. In this paper, a structured approach is developed to obtain a low-dimensional dynamic model for a laminar absolutely and globally unstable cylinder wake flow at a Reynolds number of $Re=100$. Two-dimensional CFD simulations were performed for the onset of the limit cycle oscillation, as well as various open-loop periodically forced cases. Forcing was implemented as translation of the cylinder normal to the flow. Data from all of these transient simulations were analysed using short-term proper orthogonal decomposition (SPOD) of each individual shedding cycle, using the unsteady lift

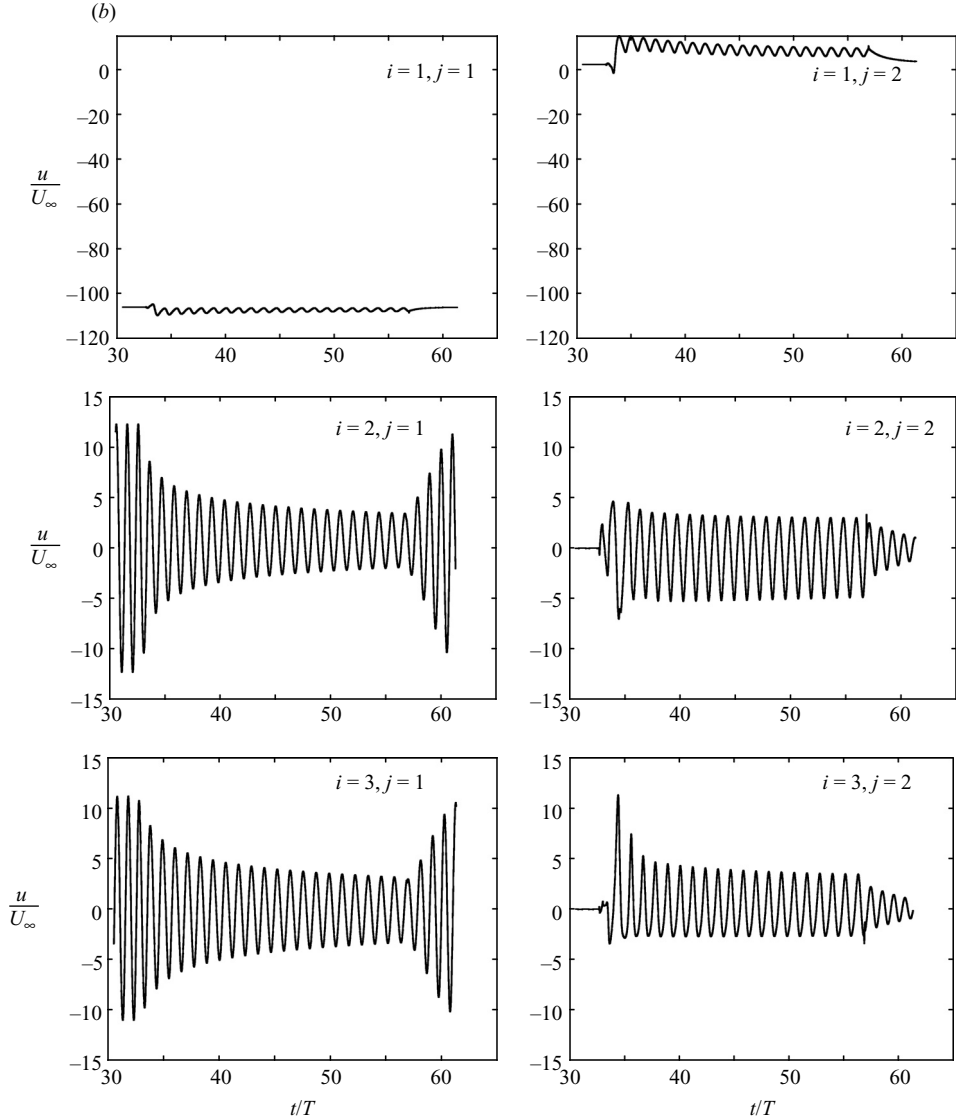


FIGURE 20. (a) Closed-loop simulation of first 6 DPOD modes (a_{ij}) using CFD simulation. Mode $a(2, 1)$ fed back through a PD controller. The P and D gains were adjusted according to mode $a(1, 1)$ amplitude. (b) Closed-loop simulation of 6 DPOD mode (a_{ij}) with the 2×3 DPOD ANN-ARX model. Mode $a(2, 1)$ fed back through PID controller to create a closed-loop simulation. Although no closed-loop data were used to train the network, mode amplitudes qualitatively match CFD closed-loop simulations in (a).

force to segment the data sets into individual shedding cycles. These short-term POD spatial modes were then subjected to a second POD decomposition to obtain an energy optimal representation of each main mode and one or more ‘shift modes’ representing its change over time. By projecting the original data sets onto this spatial basis of DPOD modes, we obtained the mode amplitudes. A reconstruction of the flow field and comparison to the original CFD data demonstrates the ability of the obtained DPOD basis to span the entire subspace from the unforced wake through

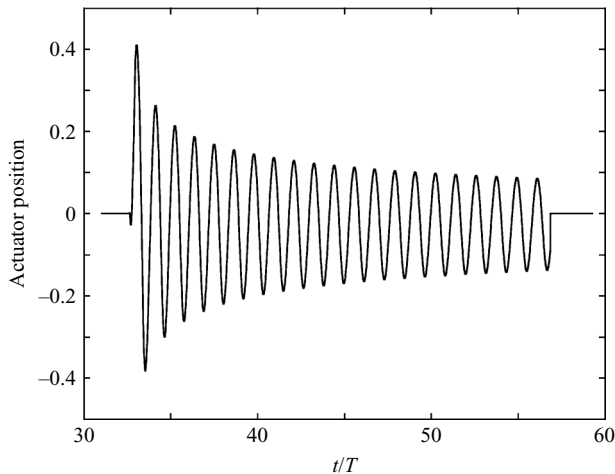


FIGURE 21. PID controller output of ANN-ARX closed-loop simulation. The PID controller gains are: $K_p = -0.45$, $K_I = -0.1$, $K_D = -2$. This is also the cylinder displacement $y(t)$.

the transient onset of vortex shedding to the open-loop forced flow conditions. Based on energy and modelling-error considerations, we truncate the DPOD basis to 5 main and 3 shift modes. The mode amplitudes obtained for the 15 DPOD modes are then used as input for nonlinear system identification.

A nonlinear ANN-ARX model was developed using a composite data set consisting of the transient development of the limit cycle as well as one open-loop forced simulation as design cases for training of the ANN within the lock-in region. The validation of the ANN for five different cases within the lock-in region provided promising results and shows accuracy as well as stability and robustness.

It is worth noting that the approach presented here is free of any assumption about the mathematical form of the equations that describe the dynamics of the flow. While it is possible to make reasonable mathematical assumptions based on first principles for relatively simple flow fields such as the cylinder wake at low Reynolds numbers, it is difficult, if not impossible, to deduce accurate equations for more complex flows. However, it is the latter class of flows which is of greatest technical interest. The approach presented here can be applied to more complex flow fields without any modifications, since it is data driven and devoid of simplifying assumptions concerning the form of the equations. This will enable the derivation of low-dimensional models for flow fields that have so far been out of reach of current modelling techniques. As long as enough transient flow-field data is available, a low-dimensional DPOD-ANN-ARX model can be derived that spans the range of flow conditions from which data were used for model development. We have shown a model that covers the open-loop and feedback-controlled flow states within the lock-in region at one set Reynolds number. We also demonstrate that by including data from a simulation increasing the Reynolds number smoothly from 40 to 100, the flow at Reynolds numbers within that range is modelled correctly. Thus, we have demonstrated that our model spans two parameters, namely forcing input with amplitude and frequency, and Reynolds number, within the range of training data used. It is possible to extend the range of validity by adding more training data for different Reynolds numbers or forcing conditions. By adding additional inputs to the model, the DPOD-ANN-ARX technique can be extended to model flow behaviour

that depends on additional parameters, for example multiple actuators. Since the entire modelling procedure does not depend on the details of the source data (e.g. the numerical grid or boundary conditions), it should be possible to adapt it to more complex flow geometries without modifications.

The approach presented here is a systematic procedure involving transient data collection, followed by derivation of DPOD modes that are accurate for all of the underlying flow states. The mode amplitudes are then used to train an artificial neural network using system identification methods. The resulting network is static and represents the flow dynamics for all transient flow states used in its derivation. The resulting model is small in numerical terms and cost efficient to solve, enabling real-time implementation for feedback control.

8. Outlook

So far we have demonstrated the applicability of our modelling approach to the benchmark problem of a two-dimensional circular cylinder wake at a Reynolds number of 100. At one reviewer's request we discuss in this section the applicability of the method to more complex flows. While we aim to avoid unsupported speculation as much as possible, we find it beneficial to share some insight we have gained into this issue from preliminary investigations.

The circular cylinder wake at $Re = 100$ is not an entirely two-dimensional flow, as has been shown in the literature for example by Williamson (1996) for the unforced wake, or by Seidel *et al.* (2006) for the feedback-controlled wake. The latter investigation demonstrates how feedback control can cause a spanwise phase shift of the vortex shedding until the two-dimensional-control approach is effective only in the narrow vicinity of the two-dimensional sensing plane that was used in this investigation. This poses the question of whether the DPOD-ANN-ARX approach can be extended to three-dimensional flows. The answer is an unequivocal yes, since there is no limitation of the DPOD decomposition to two dimensions, as was pointed out in §3.

As the Reynolds number of the circular cylinder flow is increased beyond $Re \sim 180$, secondary instabilities lead to the formation of streamwise vortices (Williamson 1996). While modelling these flow features will lead to additional DPOD modes, there is no apparent obstacle to applying POD-based modelling to flow fields that contain both two- and three-dimensional features, as has been shown in the hybrid approach proposed by Ma & Karniadakis (2002). Extending their work to use the DPOD procedure introduced here, we could derive dynamic models capturing the effect of actuation and/or changes in Reynolds number for these types of flow. This could then be used to develop feedback controllers to suppress the von Kármán type vortex shedding. Based on results of Cohen *et al.* (2003), where feedback of the von Kármán mode suppressed only higher-order harmonic modes, there is hope that suppressing the Kármán vortex street might eliminate the streamwise vortices as well, since they are the result of a secondary instability that exists only in the presence of the von Kármán vortex shedding. Whether this conjecture is in fact true remains to be shown.

At yet higher Reynolds numbers ($Re > 3900$), the von Kármán vortices break down into smaller and smaller turbulent structures that ultimately dissipate their energy into heat. These smaller structures can be quite energetic and thus more and more POD modes must be retained in order to model a given fraction of the overall flow energy content. This behaviour of POD is due to the energy optimality of the procedure, and DPOD inherits this property from POD. As a result, both POD and DPOD models will become inherently large for flows that break down into

turbulence. If the purpose of model development is feedback control, however, there may not be a need to model the small turbulent eddies in order to capture the dynamic behaviour of the large vortical structures. In the case of the circular cylinder wake, we may be interested only in modelling the von Kármán type shedding for the reasons outlined in the previous paragraph. Thus, an approach where the flow data is subjected to either spatial or temporal filtering may be applied, as has been pursued with good preliminary results (Siegel *et al.* 2007). The approach proposed in this work removes small-scale turbulent structures from the data used for POD mode derivation while retaining the large structures (i.e. von Kármán vortices) that are of interest for feedback-controller development. This approach is much like the use of spatial filtering in large-eddy simulations employed in state-of-the-art CFD solvers. With this approach, we introduce a choice of how much or how little of the smaller structures are included in the model. Thus, we can derive models with relatively few modes that nonetheless capture the dynamics of the flow that is relevant for feedback control. The DPOD-ANN-ARX approach is particularly suited to this type of modelling, since no turbulence model is required. As the entire model development is data driven and does not include projection onto the Navier–Stokes equations, no closure equations are required. The approach can thus be used as introduced here, with the only added step being a filtering process before the derivation of the DPOD modes. However, more detailed investigations into filter kernel type, size and cutoff wavelength are needed.

An important question pertaining to the application of DPOD to flow fields with multiple equally dominant frequencies is the selection of appropriate bin boundaries. In the present investigation, higher-frequency content was small in amplitude compared to the fundamental frequency of the vortex shedding, and thus the lift force with a simple peak detection algorithm was suitable for bin segmentation, as shown in figure 3. If several dominant frequencies coexist, there are different possible approaches to segmentation. Using a phase accurate temporal notch filter as a pre-processing step, we may recover the fundamental frequency and determine bin boundaries in the same fashion as introduced in this work. Alternatively, it is conceivable to use open-loop forcing to elevate the amplitude of one of the dominant frequencies at a time, thus allowing for discovery of the spatial flow features related to each frequency using multiple SPOD procedures, one for each of the frequencies of interest.

Having outlined possible pathways of how the DPOD-ANN-ARX approach may be applied and extended to flow fields at Reynolds numbers of technical interest, the question remains as to how applicable this approach may be to other flow geometries. We consider the circular cylinder wake as a prototype flow featuring separated free shear layers that develop instabilities leading to vortex shedding. As such, there are similarities to many other flows of technical interest that contain free shear layers, featuring both simpler and more complex flow behaviour. Examples that we have investigated are the separated flow over a stalled airfoil, free shear layers formed behind a D shaped cylinder, and the wake of an axisymmetric bluff body. Although we have yet to apply the DPOD-ANN-ARX approach to these flows, we consider them promising candidates since they all feature large coherent structures resulting from instabilities. The interaction of these instabilities and their resulting structures with flow actuators of various kinds is of great technical interest, both for open- and closed-loop flow control. DPOD-ANN-ARX models may be used to investigate this interaction in a structured and quantitative fashion.

In summary, we developed this approach with the intent to use the resulting models for controller development in order to achieve control of the formation

of large structures caused by flow instabilities. From a technical perspective, these types of flow are the most promising candidates for feedback flow control since instabilities can be influenced with relatively small amounts of actuation energy. This is important in the context of the power limitations inherent in state-of-the-art dynamic flow actuators. Our approach supports flow fields with many different modes present, and can also accommodate multiple actuator interaction allowing for MIMO control. We did not intend it to be used for random turbulent flows, but find that there are many technical applications where this limitation is of no importance.

The authors would like to acknowledge the support and assistance provided by Lt Col Sharon Heise and Lt Col Scott Wells from the Air Force Office of Scientific Research and Dr James Myatt of the Air Force Research Laboratories. This effort was also supported by Dr Jim Forsythe of Cobalt Solutions, LLC. The authors appreciate the fruitful discussions with Dr Young Sug-Shin on system identification using artificial neural networks and for his very helpful insight. We would like to thank Dr Mark Balas for his support and fruitful discussions.

REFERENCES

- AFANASIEV, K. & HINZE, M. 2001 *Adaptive Control of a Wake Flow Using Proper Orthogonal Decomposition. Shape Optimization and Optimal Design*. Lecture Notes in Pure and Applied Mathematics, vol. 216. Springer.
- ALBAREDE, P. & MONKEWITZ, P. A. 1992 A model for the formation of oblique shedding patterns and chevrons in cylinder wakes. *Phys. Fluids A* **4**, 744–756.
- BERGMANN, M. & CORDIER, L. 2006 Control of the cylinder wake in the laminar regime by trust-region methods and POD reduced-order models. Preprint.
- BERGMANN, M., CORDIER, L. & BRANCHER, J. P. 2005 Optimal rotary control of the cylinder wake using POD reduced order model. *Phys. Fluids* **17**(9), 357–392.
- CHOMAZ, J. M., HUERRE, P. & REDEKOPP, L. G. 1988 Bifurcations to local and global modes in spatially developing flows. *Phys. Rev. Lett.* **60** (1), 25–28.
- COHEN, K., SIEGEL, S., MCLAUGHLIN, T. & GILLIES, E. 2003 Feedback control of a cylinder wake low-dimensional model. *AIAA J.* **41**, 1389–1391.
- COHEN, K., SIEGEL, S., SEIDEL, J. & MCLAUGHLIN, T. 2006 System identification of a low dimensional model of a cylinder wake. *AIAA Paper* 2006-1411.
- CYBENKO, G. V. 1989 Approximation by superpositions of a sigmoidal function. *Maths Control Signals Syst.* **2**, 303–314.
- DEANE, A. E., KEVREKIDIS, I. G., KARNIADAKIS, G. E. & ORSZAG, S. A. 1991 Low-dimensional models for complex geometry flows: application to grooved channels and circular cylinders. *Phys. Fluids* **3**(10), 2337–2354.
- EFE, M. Ö., DEBIASI, M., ÖZBAY, H. & SAMIMY, M. 2004 Modeling of subsonic cavity flows by neural networks. In *Intl Conf. Mechatronics (ICM)*, Istanbul, Turkey, 560–565.
- EFE, M. Ö., DEBIASI, M., YAN, P., ÖZBAY, H. & SAMIMY, M. 2005 Control of subsonic cavity flows by neural networks – analytical models and experimental validation. *AIAA Paper* 2005-0294.
- FAHL, M. 2000 Trust-region methods for flow control based on reduced order modeling. PhD thesis, Trier university.
- FALLER, W. E. & SCHRECK, S. J. 1997 Unsteady fluid mechanics applications of neural networks. *J. Aircraft* **34**, 48–55.
- FALLER, W. E., SCHRECK, S. J. & LUTIGES, M. W. 1995 Neural network prediction and control of three-dimensional unsteady separated flowfields. *J. Aircraft* **32**, 1213–1220.
- FAN, X. 1995 Laminar flow control models with neural networks. PhD thesis, Ohio State University, Columbus, Ohio.
- FAN, X., HOFMANN, L. & HERBERT, T. 1993 Active flow control with neural networks. *AIAA Paper* 1993-3273.

- GAD-EL-HAK, M. 2000 *Flow Control: Passive, Active, and Reactive Flow Management*, pp. 352–357. Cambridge University Press.
- GALLETTI, B., BRUNEAU, C. H., ZANNETTI, L. & IOLLO, A. 2004 Low-order modelling of laminar flow regimes past a confined square cylinder. *J. Fluid Mech.* **503**, 161–170.
- GERHARD, J., PASTOOR, M., KING, R., NOACK, B. R., DILLMANN, A., MORZYNSKI, M. & TADMOR, G. 2003 Model based control of vortex shedding using low-dimensional galerkin models. *AIAA CP* 2003-4261.
- GILLIES, E. A. 1995 Low-dimensional characterization and control of non-linear wake flows. PhD dissertation, Faculty of Engineering, University of Glasgow, UK.
- GILLIES, E. A. 1998 Low-dimensional control of the circular cylinder wake. *J. Fluid Mech.* **371**, 157–178.
- GILLIES, E. A. 2000 Multiple sensor control of vortex shedding. *AIAA Paper* 2000-1933.
- GLEZER, A., KADIOGLU, Z. & PEARLSTEIN, A. J. 1989 Development of an extended proper orthogonal decomposition and its application to a time periodically forced plane mixing layer. *Phys. Fluids A* **1**(8).
- GOTTLIEB, J. J. & GROTH, C. P. T. 1988 Assessment of Riemann solvers for unsteady one-dimensional inviscid flows of perfect gases. *J. Comput. Phys.* **78**(2), 437–458.
- GRAHAM, W. R., PERAIRE, J. & TANG, K. Y. 1999a Optimal control of vortex shedding using low-dimensional models. Part I: Open-loop model development. *Intl J. Numer. Meth. Engng* **44**, 945–972.
- GRAHAM, W. R., PERAIRE, J. & TANG, K. Y. 1999b Optimal control of vortex shedding using low-dimensional models. Part II: Model based control. *Intl J. Numer. Meth. Engng* **44**, 973–990.
- HAYKIN, S. 1999 *Neural Networks – A Comprehensive Foundation*, 2nd edn. Prentice-Hall.
- HOČEVAR, M., ŠIROK, B. & GRABEC, I. 2004 Experimental turbulent field modeling by visualization and neural networks. *Trans. ASME* **126**, 316–322.
- HOLMES, P., LUMLEY, J. L. & BERKOOZ, G. 1996 *Turbulence, Coherent Structures, Dynamical Systems and Symmetry*. Cambridge University Press.
- HUERRE, P. & MONKEWITZ, P. 1990 Local and global instabilities in spatially developing flows. *Annu. Rev. Fluid Mech.* **22**, 473–537.
- JØRGENSEN, B. H., SØRENSEN, J. N. & BRØNS, M. 2003 Low-dimensional modeling of a driven cavity flow with two free parameters. *Theoret. Comput. Fluid Mech.* **16**(4), 299–317.
- VON KÁRMÁN, T. 1954 *Aerodynamics: Selected Topics in Light of their Historic Development*. Cornell University Press.
- VON KÁRMÁN, T. 1911 Über den Mechanismus des Widerstands, den ein bewegter Körper in einer Flüssigkeit erfährt. *Nachr. Ges. Wiss. Göttingen, Math. Phys. Kl.*, 509–517.
- KHIBNIK, A. I., NARAYANAN, S., JACOBSON, C. A. & LUST, K. 2000 Analysis of low dimensional dynamics of flow separation. *Proc. ERCOFTAC/EUROMECH Colloquium 383 Aussois, France, 1998*. Vieweg.
- KOOPMANN, G. 1967 The vortex wakes of vibrating cylinders at low reynolds numbers. *J. Fluid Mech.* **28**, 501–512.
- LEE, C., KIM, J., BABCOCK, D. & GOODMAN, R. 1997 Application of neural networks to turbulence control for drag reduction. *Phys. Fluids* **9**(6), 1740–1747.
- LJUNG, L. 1999 *System Identification – Theory for the User*, 2nd edn. Prentice-Hall.
- LUCHTENBURG, M., TADMOR, G., LEHMANN, O., NOACK, B. R., KING, R. & MORZYNSKI, M. 2006 Tuned POD Galerkin models for transient feedback regulation of the cylinder wake. *AIAA Paper* 2006-1407.
- MA, X. & KARNIADAKIS, G. 2002 A low-dimensional model for simulating three-dimensional cylinder flow. *J. Fluid Mech.* **458**, 181–190.
- MIN, C. & CHOI, H. 1999 Suboptimal feedback control of vortex shedding at low Reynolds numbers. *J. Fluid Mech.* **401**, 123–156.
- MORZYNSKI, M., STANKIEWICZ, W., NOACK, B. R., THIELE, F. & TADMOR, G. 2006 Generalized mean-field model for flow control using continuous mode interpolation. *AIAA Paper* 2006-3488.
- NARAYANAN, S., KHIBNIK, A. I., JACOBSON, C. A., KEVEREKEDIS, Y., RICO-MARTINEZ, R. & LUST, K. 1999 Low-dimensional models for active control of flow separation. *Proc. 1999 IEEE Intl Conf. on Control Applications, Kohala Coast-Island of Hawaii, Hawaii, USA*, pp. 1151–1156.
- NELLES, O. 2001 *Nonlinear System Identification*. Springer.

- NOACK, B. R., OHLE, F. & ECKELMANN, H. 1991 On cell formation in vortex streets. *J. Fluid Mech.* **227**, 293–308.
- NOACK, B. R., AFANASIEV, K., MORZYNSKI, M. & THIELE, F. 2003 A hierarchy of low-dimensional models for the transient and post-transient cylinder wake. *J. Fluid Mech.* **497**, 335–363.
- NOACK, B. R., TADMOR, G. & MORZYNSKI, M. 2004a Low-dimensional models for feedback flow control. Part I: Empirical Galerkin models. *AIAA Paper* 2004-2408.
- NOACK, B. R., TADMOR, G. & MORZYNSKI, M. 2004b Actuation models and dissipative control in empirical Galerkin models of fluid flows. *American Control Conf. Boston, MA, USA*, Paper FrP15.6.
- NØRGAARD, M., RAVN, O., POULSEN, N. K. & HANSEN, L. K. 2000 *Neural Networks for Modeling and Control of Dynamic Systems*. Springer.
- OERTEL, H. JR 1990 Wakes behind blunt bodies. *Annu. Rev. Fluid Mech.* **22**, 539–564.
- PANTON, R. L. 1996 *Incompressible Flow*, 2nd edn. John Wiley.
- PAPANGELOU, A. 1992 Vortex shedding from slender cones at low Reynolds numbers. *J. Fluid Mech.* **242**, 299–321 (and Corrigendum **248**, 1993, 684).
- PARK, D. S., LADD, D. M. & HENDRICKS, E. W. 1993 Feedback control of a global mode in spatially developing flows. *Phys. Lett. A* **182**–244.
- PINDERA, M. Z. 2002 Adaptive flow control using simple artificial neural networks. *AIAA Paper* 2002-0990.
- RAVINDRAN, S. 2000 Reduced-order adaptive controllers for fluid flows using POD. *J. Sci. Comput.* **15**, 457–478.
- REMPFER, D. 2000 On low-dimensional Galerkin models for fluid flow. *Theoret. Comput. Fluid Mech.* **14**(2), 75–88.
- ROUSSOPOULOS, K. 1993 Feedback control of vortex shedding at low Reynolds numbers. *J. Fluid Mech.* **248**, 267–296.
- ROUSSOPOULOS, K. & MONKEWITZ, P. A. 1996 Nonlinear modeling of vortex shedding control in cylinder wakes. *Physica D* **97**, 264–73.
- SAHAN, R. A., KOC-SAHAN, N., ALBIN, D. C. & LIAKOPOULOS, A. 1997 Artificial neural network based modeling and intelligent control of transitional flows. *Proc. 1997 IEEE Intl Conf. on Control Applications, Hartford, CT*, pp. 359–364.
- SEIDEL, J., SIEGEL, S., COHEN, K., BECKER, V. & McLAUGHLIN, T. 2006 Simulations of three dimensional feedback control of a circular cylinder wake. *AIAA Paper* 2006-1404.
- SIEGEL, S., COHEN, K. & McLAUGHLIN, T. 2003 Feedback control of a circular cylinder wake in experiment and simulation (Invited). *AIAA Paper* 2003-3569.
- SIEGEL, S., COHEN, K. & McLAUGHLIN, T. 2004 Feedback control of a circular cylinder wake in a water tunnel experiment. *AIAA Paper* 2004-0580.
- SIEGEL, S. G., COHEN, K., SEIDEL, J. & McLAUGHLIN, T. 2005 Short time proper orthogonal decomposition for state estimation of transient flow fields. *AIAA Paper* 2005-0296.
- SIEGEL, S., COHEN, K. & McLAUGHLIN, T. 2006 Numerical simulations of a feedback controlled circular cylinder wake. *AIAA J.* **44**(6), 1266–1276.
- SIEGEL, S., ARADAG, S., SEIDEL, J., COHEN, K. & McLAUGHLIN, T. 2007 Low dimensional POD based estimation of a 3D turbulent separated flow. *AIAA Paper* 2007-0112.
- SIRISUP, S., KARNIADAKIS, G. E., XIU, D. B. & KEVREKIDIS, I. G., 2005 Equation-free/Galerkin-free POD-assisted computation of incompressible flows. *J. Computat. Phys.* **207**(2), 568–587.
- SIROVICH, L., 1987 Turbulence and the dynamics of coherent structures. Part I: Coherent structures. *Q. Appl. Maths* **45**(3), 561–590.
- STRANG, W. Z., TOMARO, R. F. & GRISMER, M. J. 1999 The defining methods of Cobalt60: a parallel, implicit, unstructured Euler/Navier–Stokes flow solver. *AIAA Paper* 99-0786.
- STUART, J. T. 1958 On the non-linear mechanics of hydrodynamic stability. *J. Fluid Mech.* **4**, 1–21.
- TADMOR, G., NOACK, B. R., MORZYNSKI, M. & SIEGEL, S. 2004 Low-dimensional models for feedback flow control. Part II: Observer and controller design. *AIAA Paper* 2004-2409.
- TAYLOR, J. A. & GLAUSER, M. N. 2004 Towards practical flow sensing and control via POD and LSE based low-dimensional tools. *Trans. ASME I: J. Fluids Engng* **16**(3), 337–345.
- WILLIAMSON, C. H. K. 1996 Vortex dynamics in the cylinder wake. *Annu. Rev. Fluid Mech.* **28**, 477–539.
- ZIELINSKA, B. J. A. & WESFREID, J. E. 1995 On the spatial structure of global modes in wake flow. *Phys. Fluids* **7**(6), 1418–1424.